Monthly Notices
of the
ROYAL ASTRONOMICAL SOCIETY

Mon. Not. R. Astron. Soc. **401,** 2499–2516 (2010) doi:10.1111/j.1365-2966.2009.15825.x

Dynamic picture of the inner asteroid belt: implications for the density, size and taxonomic distributions of real objects

T. A. Michtchenko,[1⋆] D. Lazzaro,[2] J. M. Carvano[2] and S. Ferraz-Mello[1]

[1]*Instituto de Astronomia, Geofísica e Ciências Atmosféricas, USP, Rua do Matão 1226, 05508-900 São Paulo, Brazil*
[2]*Observatório Nacional, R. Gal. José Cristino 77, 20921-400, Rio de Janeiro, Brazil*

Accepted 2009 October 2. Received 2009 October 2; in original form 2009 September 3

ABSTRACT

In this paper, we construct a dynamic portrait of the inner asteroidal belt. We use information about the distribution of test particles, which were initially placed on a perfectly rectangular grid of initial conditions, after 4.2 Myr of gravitational interactions with the Sun and five planets, from Mars to Neptune. Using the spectral analysis method introduced by Michtchenko et al., the asteroidal behaviour is illustrated in detail on the dynamical, averaged and frequency maps. On the averaged and frequency maps, we superpose information on the proper elements and proper frequencies of real objects, extracted from the data base, AstDyS, constructed by Milani and Knežević. A comparison of the maps with the distribution of real objects allows us to detect possible dynamical mechanisms acting in the domain under study; these mechanisms are related to mean-motion and secular resonances. We note that the two- and three-body mean-motion resonances and the secular resonances (strong linear and weaker non-linear) have an important role in the diffusive transportation of the objects. Their long-lasting action, overlaid with the Yarkovsky effect, may explain many observed features of the density, size and taxonomic distributions of the asteroids.

Key words: minor planets, asteroids.

1 INTRODUCTION

The dynamical structure, stability, physical composition and possible origin of the asteroidal belt have been studied exhaustively. Many problems related to these issues have been solved, mainly those concerning the dynamics of massless objects. However, we have noted that some very important features of asteroid dynamics are still ignored, even in recently published research. Thus, we have decided to construct a global dynamic picture of the main belt, combining already established facts and new results from our investigations. We begin by describing the inner part of the belt, while results concerning the middle and outer parts will be the subject of forthcoming papers.

This is not a new attempt to construct a global view of the asteroidal distribution. We refer to the relevant research, developed by Milani & Knežević during almost one decade and published in many papers (e.g. Milani & Knežević 1990, 1992, 1994; Knežević & Milani 1994, 2000, 2003. The research, which aimed to elaborate the theories (both analytical and synthetic) of proper asteroidal elements, has resulted in the creation of a data base, AstDyS. This is accessible at http://hamilton.dm.unipi.it/astdys, and is continuously updated and expanded. The importance of having an ample data base of proper elements is emphasized in the following statement by Knežević & Milani (2003): '... these data enabled us to conduct a comprehensive, yet straightforward statistical analysis of the results, and provided us with a sort of "dynamical portrait" of the main belt as a whole...'.

Although our work has strong ties to the work of Milani & Knežević, our approach is qualitatively different. Instead of working with the statistical analysis of real objects, we analyse the asteroidal dynamics using fictitious test particles. The main idea consists of the construction of maps of the asteroidal belt using information about the distribution of the test particles. These were initially placed over a perfectly rectangular grid of initial conditions, after 4.2 Myr of gravitational interactions with the Sun and five planets, from Mars to Neptune. Indeed, the final distribution of the fictitious particles will reflect the peculiarities of dynamical interactions between asteroids and the planets in the region under study. In particular, the test particles will preserve (at least, during the time-span covered by integrations) some invariable quantities of motion (e.g. proper elements), if they belong to the domains of quasi-regular motion. In contrast, these quantities will exhibit variations in the domains of dynamical instabilities, which can even result in the escape of the objects from the studied region. As we show in this paper, the test particles can form agglomerations or, in contrast, some voids in the specific regions of the phase space, as a result of the action of mean-motion resonances (MMRs) and secular

⋆E-mail: tatiana@astro.iag.usp.br

resonances (SRs), in such a way as to indicate the location of these features.

Our results, evidently, complement the data on the proper elements from AstDyS, mainly in the regions of the belt characterized by large instabilities and a lack of real objects. Moreover, our approach provides evidence of how the peculiarities in the asteroidal distribution are formed. A comparison of the maps with the distribution of real objects allows us to detect possible dynamical mechanisms acting in the domain under study. These mechanisms are related to MMRs and SRs, close encounters between asteroids and asteroids with planets, asteroidal collisions, etc.

It has already been recognized that resonances overlaid with the dissipative Yarkovsky effect (Farinella & Vokrouhlický 1999) can produce a diffusive transport of the bodies, which seems to be common in the asteroidal belt. For instance, over very long time-spans, a slow chaotic diffusion can drive members of the asteroid families out of the regions in the phase space that the family occupies (Milani & Farinella 1994; Milani, Nobili & Knežević 1997; Morbidelli & Nesvorny 1999; Carruba et al. 2005).

In this paper, we assume that the actual distribution of the asteroidal population in the inner belt is produced mainly by dynamical processes related to MMRs and SRs, both interacting with dissipative Yarkovsky effects. 'Catastrophic' events, such as the sweeping by migrating planets and/or the excitation by putative planet embryos, are not taken into consideration. This means that the lifetime of the belt considered in this work starts soon after planet formation has been completed. There are other phenomena also not considered in this work, those that provoke minor effects (such as close encounters between asteroids) or only probabilistic effects (such as collisions between asteroids).

We should emphasize that we concentrate our study on the global features of the distribution of inner belt objects and their dynamical interactions with the planets. Therefore, specific issues such as, for example, a detailed study of the existing asteroid families and simulations of diffusion of their members are not included in this work. Thus, even though the literature on asteroidal dynamics is vast, we refer only to the part related to global studies, not to investigations on specific subjects.

The methods used in this work are mainly numerical, although the analytical theory developed by Milani & Knežević (1990) has been invoked when numerical methods have not worked. The dynamic portrait of the inner belt was constructed in the form of dynamical, averaged and frequency maps, employing the spectral analysis method (hereafter SAM; Michtchenko et al. 2002). The determination of the diameters of real objects was based on the values of both absolute magnitudes available from the Bowell catalogue (ftp://ftp.lowell.edu/pub/elgb/astorb.html) and albedos available in the IRAS catalogue (Tedesco et al. 2002). Finally, information on the taxonomy of objects was extracted from the Eight-Colour Asteroid Survey (ECAS; Zellner, Tholen & Tedesco 1985), the Small Main-Belt Asteroid Spectroscopic Survey (SMASS; Burbine & Binzel 2002; Bus & Binzel 2002) and the Small Solar System Objects Spectroscopic Survey (S^3OS^2; Lazzaro et al. 2004, 2009).[1]

The paper is organized as follows. We start by analysing the asteroid distribution in the proper elements space. In Section 3, we present dynamical maps of the representative planes of the osculating elements and we compare their structure with the distribution of maximum Lyapunov characteristic exponents (LCEs), extracted from the AstDyS catalogue. The distribution of asteroids in the proper frequencies space, introduced in Section 4, is useful for the identification of MMRs and SRs present in the inner belt. In Section 5, we introduce averaged maps, which allow a direct comparison with the distribution of real objects. In the subsections, we analyse and identify the possible dynamical mechanisms responsible for the actual shape of the asteroid distribution in different eccentricity intervals. The dynamical implications for the size and taxonomic distribution of real objects are discussed in Sections 6 and 7, respectively. Finally, the results described in the paper are gathered in the summary in Section 8. We consider the questions that arise in Section 8 (and are unanswered) to be extremely important, as these may motivate further investigations.

[1] See also http://www.psi.edu/pds/asteroid.

2 ASTEROIDAL DISTRIBUTION IN THE PROPER ELEMENTS SPACE AND DYNAMICAL FAMILIES

At present, there are around 200 000 numbered objects in the Bowell catalogue of asteroid orbital elements (Bowell, Muinonen & Wasserman 1994). Of these, there are about 170 000 proper elements available in the data base AstDyS (Knežević & Milani 2003). Hereafter, we distinguish between osculating elements ($a_{\rm osc}$, $e_{\rm osc}$ and $I_{\rm osc}$) given in the Bowell data base and the proper elements (a, e and I) given in AstDyS.

About 60 000 objects are found in the range 2.1–2.5 au of the proper semimajor axis. This region of the main belt is often referred to as the inner part. The natural borders of its semimajor axis are formed by the very strong ν_6 SR (inner border) and the 3/1 MMR with Jupiter (outer border). The upper limits of eccentricities and inclinations are constrained by the strong ν_{16} SR, and a considerable amount of the objects exist up to 0.3 in proper eccentricities and 30° in proper inclinations.

To show the distribution of the asteroids in the three-dimensional proper elements space, we follow the approach used by Milani & Knežević (1992). The sample of objects is separated in different eccentricity intervals and each is presented on the (a, I)-plane of the proper semimajor axis and inclination. Hereafter, we refer to this plane as the 'representative plane'. We have chosen arbitrarily five eccentricity intervals, as described below. In each interval, we have identified one known dynamical family of asteroids and we have associated the name of this family to the interval. We have also used the values of the osculating eccentricity and angular elements of the main object of the family as the input of numerical integrations, to construct the dynamical and averaged maps. Obviously, it is possible that in a given eccentricity interval there is no asteroid family, or there are many families. However, as we are working mainly in the proper elements space, the choice of the main object associated with the interval is irrelevant.

The first interval is characterized by very low eccentricities, less than 0.075. There are neither known families nor clusters here, so we select one large object from this interval, 230 Athamantis with magnitude 7.3, and associate it with this interval. The next interval is centred around 4 Vesta and covers low-to-moderate eccentricities within the range $0.075 \leq e < 0.125$. The next two intervals are associated with 298 Baptistina and 163 Erigone, and cover the moderate ($0.125 \leq e < 0.175$) and high ($0.175 \leq e < 0.225$) eccentricities, respectively. Finally, the very-high-eccentricity region ($e \geq 0.225$) is associated with 25 Phocaea. Because of the peculiarities of the distribution of highly eccentric orbits, this last interval is studied separately, while the others are always presented together, for purposes of comparison.

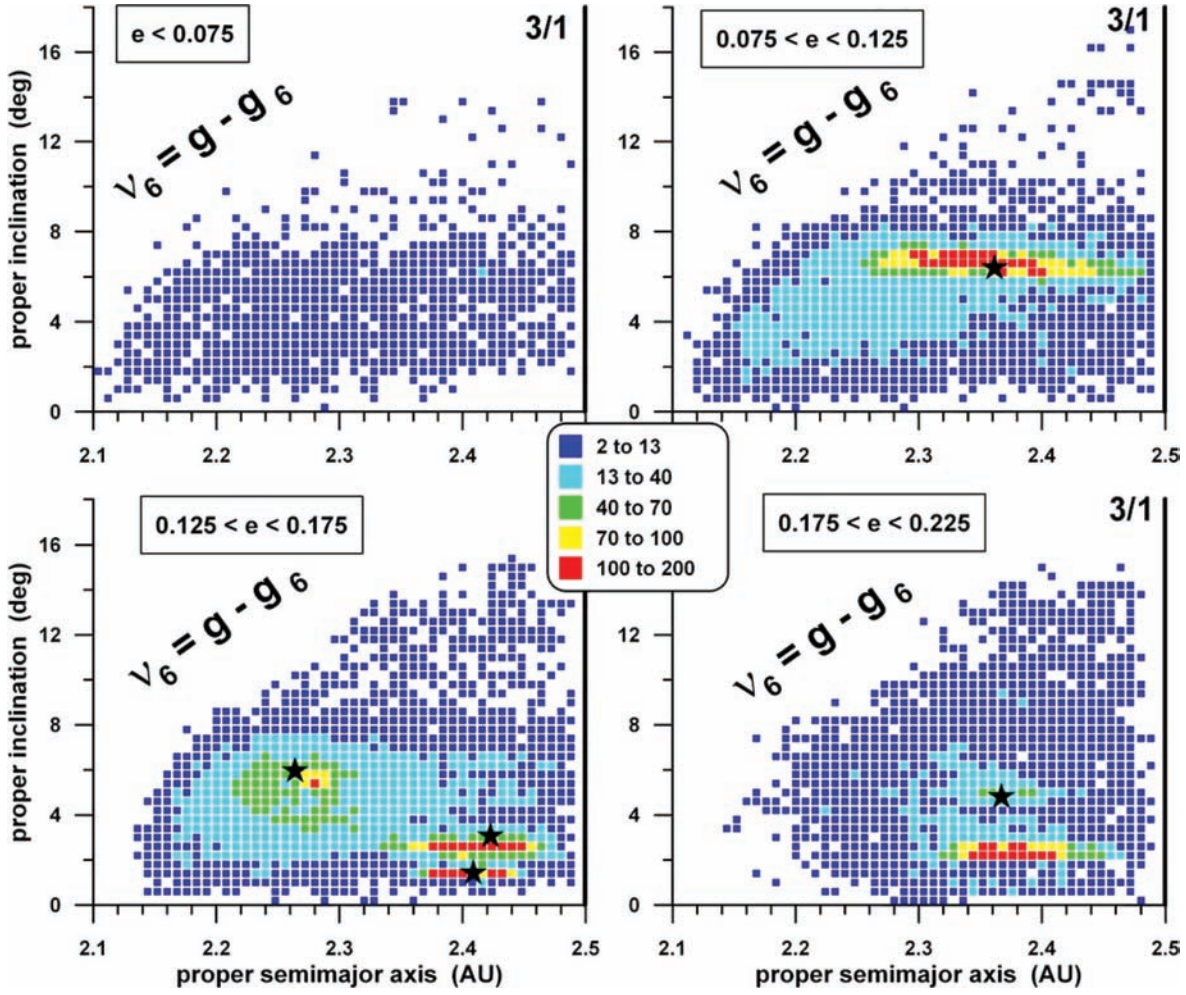

Figure 1. Density distribution of inner belt objects in the proper elements space. The corresponding eccentricity interval is indicated at the top of each panel. The density (the number of asteroids inside a cell) is shown using different colours (see the legend box): blue corresponds to minimal values (<13) and red to maximal values (>100). The size of the cell on the (a, I)-plane is 0.008 au $\times$ 0.°4. Stars indicate the locations of the main objects of the detected families.

The asteroidal distribution in the proper elements space is shown in Fig. 1. In this paper, instead of the commonly used view of the individual objects, we present an asteroidal 'density index'. The density index was calculated in the following way. Each (a, I)-plane was divided into rectangular cells of dimension 0.008 au $\times$0.°4. The number of real objects inside each cell was calculated and associated with this cell. It should be noted that the density presentation is analogous to the averaging process of the real object distribution and depends on the chosen size of the cell. We have tested several sizes and have found that the one chosen is most appropriate; it is neither too small to depict the unnecessary details of the asteroid distribution, nor too large to lose its main features.

The density indices obtained are shown in Fig. 1 on four representative planes corresponding to different eccentricity intervals. Colours represent the ranges of density index, shown in the legend box. The colour red is used to indicate the cells of the highest density detected in the inner belt, with more than 100 objects per cell. The first feature that can be clearly observed in Fig. 1 is the very low density of real objects on nearly circular orbits (top-left panel). The maximal value that the density index reaches inside this region is equal to 13 objects per cell; moreover, only one cell (in cyan) shows this value. The small values of the density index in the very-low-eccentricity region indicate the absence of agglomerations, such as dynamical families, clusters or groups. Therefore, we have chosen a density index less than 13 as typical of the background, and we show this in blue.

The absence of clusters in the very low proper eccentricity part of the inner belt is a puzzling feature of the asteroidal distribution. The low collision probability of objects in near-circular orbits seems to be a possible explanation, but the presence of small eccentricity families in the middle and outer parts of the main belt leads to doubts about the reliability of this explanation. Another incomprehensible feature at $e < 0.075$ (top-left panel of Fig. 1) is the sudden decrease of the asteroid density at $I > 8°$. However, as shown in Section 5.1, the dynamics in this region allows regular behaviour up to $I \simeq 16°$, where the strong ν_6 SR shapes the upper boundary of the asteroid population.

The picture changes at larger eccentricities. The plane centred around 4 Vesta (top-right panel of Fig. 1) is dominated by the associated family. The object 4 Vesta, shown by a star, is close to the region of the highest density (shown in red), with the maximal value of the index equal to 160 per cell. The domains of the high and intermediate densities (cells shown in yellow and green) are confined to the narrow horizontal region on the (a, I)-plane. This indicates that the dispersion of the Vesta family in inclination is significantly smaller than in the semimajor axis. This feature can be

understood in the context of orbital dynamics. To change the plane of its orbits, a particle must gain several orders more kinetic energy than that necessary to change its semimajor axis and eccentricity. In addition, the Yarkovsky dissipation enhances the dispersion of the objects in the semimajor axis. As seen later, the shape of a family on the (a, I)-plane, confined in inclination and dispersed in the semimajor axis, is typical and in agreement with results of the hydrocode simulations of family-forming events (Michel, Benz & Richardson 2004).

Curiously, the region shown by cyan squares appears to be asymmetric in the top-right panel of Fig. 1. This effect may be a result of the arbitrary division in eccentricity intervals, which provokes a leaking of the asteroidal agglomerations from one interval to another. In addition, a sudden decay of the population, for $I > 10^\circ$, is also observed at low-to-moderate eccentricities.

The next panel, constructed in the interval $0.125 \leq e < 0.175$ around 298 Baptistina, reveals the existence of several groups at moderate eccentricities (the bottom-left panel of Fig. 1). The high-density regions on the right-hand side are associated with two known families, 20 Massalia and 44 Nysa, aligned along $I = 1\overset{\circ}{.}4$ and $I = 2\overset{\circ}{.}6$, respectively. The family of 20 Massalia is the most concentrated group of the inner belt; its density index reaches its maximal value of 186 per cell, at $a = 2.4$ au and $I = 1\overset{\circ}{.}4$.

The proper eccentricity of 44 Nysa (equal to 0.174) is very close to the upper limit of the chosen eccentricity interval and the associated family extends into the next plane, covering the domain of high eccentricities (the bottom-right panel of Fig. 1). In contrast with the Massalia family, the object 44 Nysa, with proper $a = 2.423$ au and $I = 3\overset{\circ}{.}06$, is far from the centre of the associated family, whose density reaches the value 180 at $a = 2.37$ au and $I = 2\overset{\circ}{.}2$.

The object 298 Baptistina is located at $a = 2.264$ au and $I = 5\overset{\circ}{.}96$ in the bottom-left panel of Fig. 1. The contour of the asteroidal agglomeration around it contrasts with the shapes of the other families, characterized by low dispersion in inclinations. The wide dispersion of the Baptistina group is a curious feature, suggesting different dynamical mechanisms acting in the region. In addition, 298 Baptistina itself is far away from the centre ($a = 2.28$ au and $I = 5\overset{\circ}{.}4$) of the highest density (106 objects per cell) associated with its group.

As seen in the bottom-left panel of Fig. 1, the domain with inclinations higher than 10° starts to be populated at moderate eccentricities. For higher eccentricities (the bottom-right panel), the background objects (blue colour) are distributed nearly uniformly inside the borders defined by the ν_6 SR and the 3J/1A MMR. Despite the dominant presence of the Nysa family at low inclinations, only the 163 Erigone group, at $I = 5^\circ$, is observable in this region. It is not dense and its contour is irregular.

3 DYNAMICAL MAPS ON THE REPRESENTATIVE PLANES

It is nowadays accepted that many features of the asteroid distribution observed in Fig. 1 may be explained by long-lasting actions of dynamical mechanisms, present in the inner main belt. With the aim of identifying these mechanisms, we produce a dynamic portrait of the inner belt using several tools, such as dynamical and averaging maps, dynamical spectra, presentation in the frequencies space, etc. (details can be found in Michtchenko et al. 2002).

We start the analysis by constructing dynamical maps on the representative $(a_{\rm osc}, I_{\rm osc})$-planes. For this task, we employed the SAM described in Michtchenko et al. (2002). 60 300 massless particles were chosen in each eccentricity interval; their initial semimajor axes and inclinations are distributed over a rectangular 201×300 grid, covering the representative plane. Each particle has been integrated over 4.2 Myr, accounting for planetary perturbations from Mars to Neptune. The initial values of the eccentricity and initial angular elements, Ω, ϖ and λ, of the test orbits have been fixed at those of the object chosen to represent the plane. During the integration, a low passband digital filter has been applied to remove short-period oscillations of the order of orbital periods.

The output series of filtered elements for each test orbit have been Fourier analysed, in order to identify the relevant peaks in their Fourier spectra. The number of relevant peaks in the semimajor axis variation, known as a 'spectral number N', was used to characterize the chaoticity of the orbit. For regular orbits with small values of N, a few well-defined lines appear in the spectra, while for chaotic orbits the number of peaks (consequently, N) is huge. This information has been translated to a grey-scale code and plotted on the $(a_{\rm osc}, I_{\rm osc})$-planes of the osculating semimajor axis and inclination.

Fig. 2 shows the dynamical maps of the inner main belt plotted on planes corresponding to different eccentricity intervals. Because the variation of the asteroidal semimajor axis is strongly affected by MMRs, its time evolution was chosen as a basis for the calculation of N. The calculated values of N, in the range from 1 to 80, are coded in grey-scale varying logarithmically from white ($\log N = 0$) to black ($\log N = 1.9$). Large values of N indicate the onset of chaos, while lighter regions on the dynamical maps correspond to regular motion, and darker tones indicate increasingly chaotic motion. The domains where the test particles escape from the region within the time interval of integration ($\sim$4.2 Myr) are shown as hatched.

On the dynamical maps in Fig. 2 we superpose proper elements of some real objects from the corresponding eccentricity range. Only large objects are shown, those with absolute magnitudes lower than 10 (red stars) and between 10 and 12 (green stars). It is worth emphasizing that the dynamical map constructed over a grid of osculating orbital elements cannot be directly compared to the proper elements of the asteroids. Thus, Fig. 2 provides only an estimation of the dynamical distribution of real objects.

The dominant effects on the asteroidal motion are produced by the strong SRs, ν_6 and ν_{16}. The ν_6 SR occurs in the regions where the precessional rate of the asteroid's longitude of perihelion equals the precessional rate of Saturn's perihelion. The ν_6 resonance is responsible for large-scale instabilities followed by the rapid escape of the test particles inside diagonal bands crossing all maps from the lower-left to the upper-right corners in Fig. 2. The bulk of real objects are located below this band, forming the low-inclination population.

The ν_{16} SR occurs in regions where the precessional rate of the asteroid's longitude of node equals the precessional rate of Saturn's node. The ν_{16} SR produces the large domains of chaotic motion in the high-inclination zones and forms a natural upper boundary of the asteroidal population in the inner belt. High-inclination domains of quasi-regular motion can be observed between the ν_6 and ν_{16} resonances, in each panel of Fig. 2. A curious feature is the absence of high-inclined asteroids (at least, with mag <12) at low and moderate eccentricities. This population is significant only at $e > 0.18$. The motion of the objects in this region is highly non-harmonic (later, we associate this property with the action of non-linear SRs). Despite this fact, the 25 Phocaea, 5247 Krylov and 1660 Wood groups are found inside the high-inclination zone. Because of the peculiarities of the dynamics in this region, we analyse it separately in Section 5.5.

A relevant feature clearly visible in Fig. 2 is the occurrence of several vertical stripes of chaotic motion, which are associated with

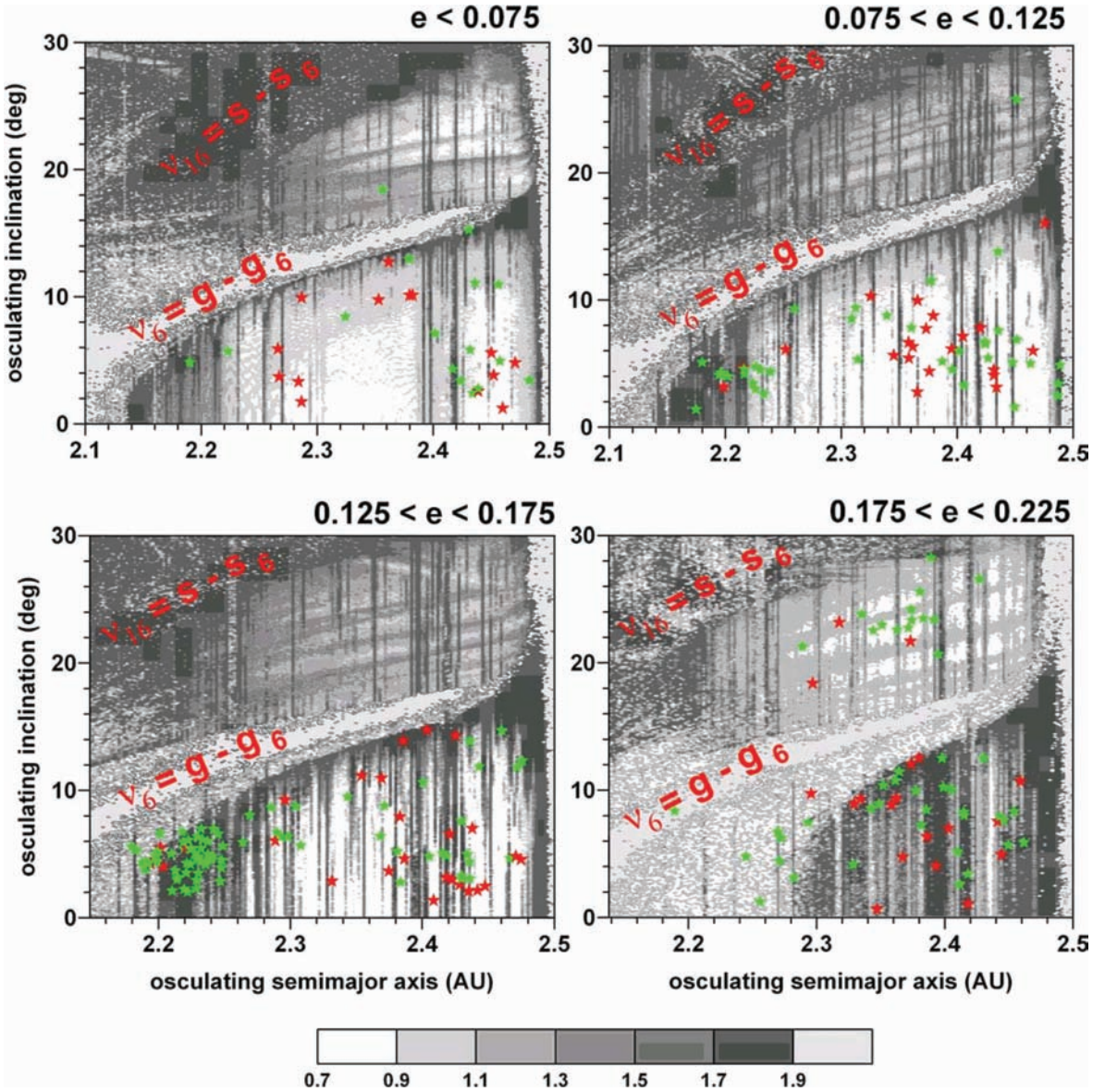

Figure 2. Dynamical maps around: 230 Athamantis (top-left panel with $e < 0.075$), 4 Vesta (top-right panel with $0.075 \leq e < 0.125$), 298 Baptistina (bottom-left panel with $0.125 \leq e < 0.175$) and 163 Erigone (bottom-right panel with $0.175 \leq e < 0.225$) on the (a, I)-planes of the osculating semimajor axis and inclination. The grey-scale levels correlate the stochasticity of motion with the spectral number N, in logarithmic scale: lighter regions correspond to regular motion, while darker tones indicate increasingly chaotic motion. The hatched regions correspond to initial conditions that lead to the escape of objects in less than 4.2 Myr. The real objects from the corresponding eccentricity interval are superposed on each graph: red stars are objects with magnitudes less than 10, while green stars are objects with magnitudes in the range 10–12.

two- and three-body MMRs with the planets from Mars to Uranus. The dominating MMR is the 3J/1A MMR with Jupiter, whose region is strongly chaotic, with rapid escapes of the test particles (the right border of all panels). Thus, the devastating effects of the 3J/1A MMR, together with ν_{16} SR, create the physical boundaries of the inner belt, while ν_6 SR delimits the domains of the low-inclination orbits.

Apart from the 3J/1A resonance, MMRs in the inner belt are weak. This is because of the large distance from the Jupiter–Saturn system and the small mass of Mars. Many of these resonances cut through the asteroid families and we can expect several family members to have been involved in the resonances. Among the most relevant are the 7J/2A MMR with Jupiter and the 1M/2A MMR with Mars. Table 1 lists the most important MMRs, in particular, several three-body MMRs of low order, such as the 4J:-1S: −1A, 4J:-2S: −1A and 5J:-4S: −1A resonances. Here, the letters J, S and A denote Jupiter, Saturn and an asteroid, respectively.

It is known that the density and the strength of the MMRs increase with increasing eccentricities. Moreover, at high eccentricities, many of them may overlap, creating the domains of unstable motion. The low-inclination region in the bottom-right panel of Fig. 2, showing high indices of stochasticity, seems to confirm this assumption. The surprising fact is that this region is significantly populated by large objects. Moreover, this population strongly contrasts with the population on nearly circular orbits (see the top-left panel of Fig. 2), which does not undergo the action of overlapping MMRs, but presents a low density of large objects.

Table 1. The groups of MMRs in the inner main belt. The resonances are presented in generic form as m_J J:m_S S : m_M M : m A, where m, m_J, m_S and m_M are integers that appear in the critical combinations of the mean motions. The letters J, S, M and A denote Jupiter, Saturn, Mars and an asteroid, respectively.

Group	Two-body resonance	Three-body resonance
1	11J/3A	9J : −4S : −2A
	3M/5A	
2	4M/7A	4J : −1S : −1A
		6J : −6S : − 1A
3	7J/2A	9J : −5S : −2A
	5M/9A	
4	6M/11A	4J : 1M : −3A
5		3J : 1S : −1A
		5J : −3M : −7A
		8J : −3S : −2A
6	10J/3A	5J : −4S : −1A
7		4J : −2S : −1A
		6J : −7S : −1A
		2J : 3S : −1A
8	1M/2A	
9		3J : 1M : −3A
		7J : −2S : −2A
		9J : −7S : −2A

To compare the behaviour of the fictitious and real objects, we use the information on stochasticity provided by maximum LCEs from the AstDyS catalogue. We separate the whole sample of real objects into two groups. One group contains objects with Lyapunov times larger than 25 000 yr, and we arbitrarily associate this value with quasi-regular motion or stable chaos (Knežević & Milani 2000). The rest of the asteroidal population, with Lyapunov times <25 000, corresponds to unstable motions. It should be emphasized that, on the one hand, it is already established that the motions of asteroids are basically chaotic, and that the dynamical mechanisms responsible for this chaos, the time-scales involved, and the size and form of the resulting macroscopic instabilities are different (Milani et al. 1997). On the other hand, the relationship between Lyapunov times (the inverse of LCEs) and the rates of chaotic diffusion is not yet clear (Morbidelli & Guzzo 1996).

The density index, defined as a fraction of the chaotic objects (with Lyapunov times <25 000) in the sample of objects inside each cell, is shown on the four representative planes in Fig. 3. Together with the information on the stochasticity of real objects, we also show the web of the resonances present in the inner belt. These are defined by vertical lines (the groups of MMRs listed in Table 1) and curves (the groups of non-linear SRs listed in Table 2). The resonances are identified and analysed in detail in the next sections. In Fig. 3, we introduce their locations, in order to compare with the distribution of chaotic orbits and the dynamical maps.

The correlation between the resonances and the chaotic behaviour of the objects can be clearly observed in the low-eccentricity domain (top-left panel) in Fig. 3, where a few cells of unstable motion stick to vertical lines representing the MMRs. For increasing eccentricities (top-right panel), the domains of chaotic orbits become larger, mainly along the 7J/2A MMR with Jupiter (group 3 in Table 1), and more dense (red and green cells in the vicinity of the ν_6 SR). The unstable motions also appear and enhance the density in the domains where the MMRs overlap with the SRs (bottom-left panel). Because the width and strength of both MMRs and SRs grow with the increasing eccentricity, the number of chaotic objects increases and reaches about half of the whole population in the high-eccentricity regions (bottom-right panel).

Finally, it is worth noting that both LCEs and the dynamical maps provide information on the so-called 'fast chaos' in the asteroidal belt. This is because of the relatively short integration times employed in their construction. The fast chaos is associated with the MMRs and the overlap of the resonances. However, the precession periods of the asteroidal perihelion and node are at least two orders of magnitude longer than the oscillation periods associated with MMRs. The total integration time is not long enough to detect the diffusive effects of non-linear SRs, and thus their visual effects are faint on the dynamical maps in Fig. 2. To analyse the chaoticity induced by non-linear SRs (often referred to as slow or stable chaos), the integration time should be increased, which will obviously significantly increase the computational costs. However, the SAM method still allows us to identify the occurrence of SRs through the construction of averaged maps (see Section 5).

4 DISTRIBUTION IN THE PROPER FREQUENCIES SPACE: MEAN-MOTION AND SECULAR RESONANCES

The previous analysis has shown that the main sources of the asteroids' chaotic behaviour are MMRs and SRs. MMRs involve the mean motions of the asteroids (n) and the planets, while the SRs involve the precession rates of the perihelia (g) and nodes (s) of the asteroids and the planets. In both cases, the proper frequencies of the asteroid motion and fundamental planetary frequencies form critical combinations (or commensurabilities).

The identification of the resonances present in the region of interest is easier when the objects are projected in the proper frequencies space (n, g, s), instead of the proper elements space. According to perturbation theories, the proper frequencies are functions of the proper elements and the transformation from these to proper frequencies is one-to-one, if the Kolgomorov non-degeneracy condition is satisfied (see Ferraz-Mello 2007). In the frequencies space, the MMRs and SRs are separable. This is because MMRs mostly depend on the proper frequency n, while SRs are linear combinations of just the proper secular g and s frequencies. It should be noted that the analysis of the asteroid distribution in the proper frequencies space is the basis for the new approach to identifying asteroid families (Carruba & Michtchenko 2007).

The nominal locations of the MMRs are easily obtained using the Kepler third law. On the (a, I)-planes, MMRs appear as vertical lines. The two- and three-body resonances form groups, which are listed in Table 1. The resonances are presented in generic form as m_J J : m_S S : m_M M : m A, where m, m_J, m_S and m_M are integers that appear in the critical combinations of the mean motions. The most important MMRs are two-body resonances with Jupiter and Mars and three-body resonances with Jupiter and Saturn. It should be stressed that, because of the small mass of Mars and the large distances to Jupiter and Saturn, we do not expect the MMRs to have a significant effect on the asteroid distribution, apart from the 3J/1A resonance with Jupiter.

As for the effects produced by the SRs, the situation is the opposite. The inner part of the main belt is a place where the SRs are very strong and dense. These resonances are visualized on the four $(g, g + s)$-planes in Fig. 4 and appear as lines (vertical, horizontal and inclined). There are four linear resonances in the inner part of the belt: two very strong SRs with Saturn, ν_6 and ν_{16}, and two weak SRs with Mars, ν_4 and ν_{14}. In particular, the ν_6 resonance separates the main bulk of the objects from the small group of highly inclined

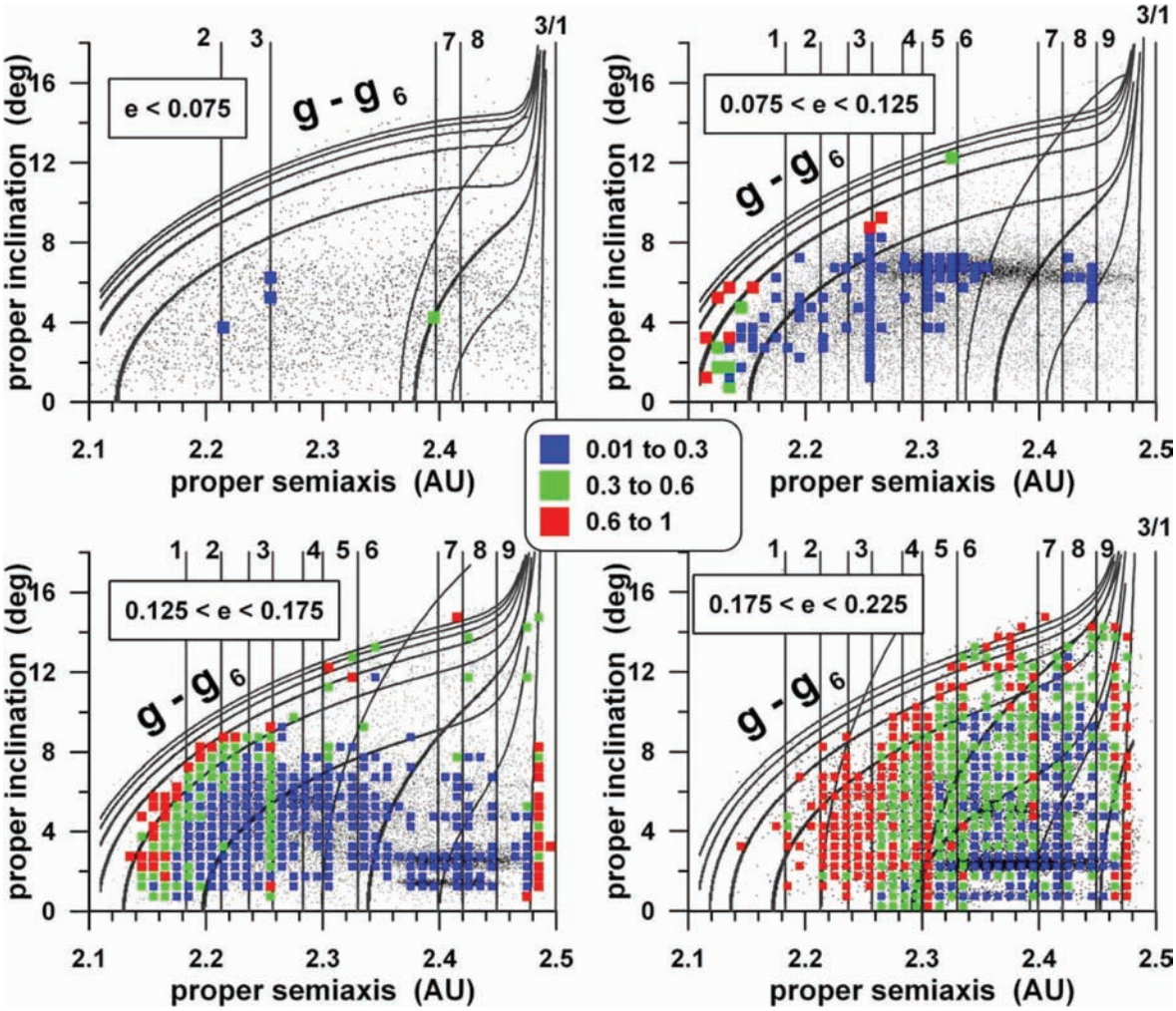

Figure 3. Density distribution of unstable orbits (with Lyapunov times <25 000 yr) in the proper elements space. The Lyapunov times are the inverse of LCEs, whose values are given in the data base of Knežević & Milani (2003). The fraction of chaotic orbits in the sample of objects inside each cell is coded by different colours (see the legend box). The size of the cell on the (a, I)-plane is 0.01 au $\times 0.^{\circ}5$. The orbits of quasi-regular motion are shown by black dots. These are 99 per cent in the Athamantis region, 97 per cent in the Vesta region, 88 per cent in the Baptistina region and 63 per cent in the Erigone region.

objects, which is observed on the dynamical maps in Fig. 1. The other important linear resonances with Jupiter and Uranus, such as ν_5, ν_7 and ν_{17}, are sufficiently close to the inner belt to produce significant dynamical effects. Their linear combinations with ν_6 and ν_{16} form SRs of higher order, known as 'non-linear SRs'.

Non-linear SRs have assumed a significant role in asteroid dynamics and any attempt to discuss the dynamical structure of the asteroid belt must take into account their effects. To obtain the non-linear SRs acting within the limits of the inner belt, we calculate all possible linear combinations that obey the resonance condition:

$$j_1\,\nu_5 + j_2\nu_6 + j_3\nu_7 + j_4\nu_4 + j_5\nu_{16} + j_6\nu_{17} + j_7\nu_{14} \cong 0.$$

Here, j_1, j_2, ... are simple integers and $\sum_i |j_i|$ is the resonance order. Table 2 lists the main non-linear resonances detected in the inner region, up to order 4. There are resonances of the g-type involving the perihelia, of the s-type involving nodes and of the gs-type involving both perihelia and nodes of the asteroid and the planets from Mars to Uranus. The resonances generally form bands, because of the peculiar relationships $g_5 \cong g_7$, $|g_6| \cong |s_{16}|$ and $|g_7| \cong |s_{17}|$.

It is evident that not all resonances will play the same role in asteroid dynamics. Among the detected non-linear resonances, two clearly exhibit the captured real objects; these are the g-type third-order $(2\nu_6 - \nu_5)$ resonance of perihelia from the g-1 group and the mixed second-order $(\nu_6 - \nu_{16})$ resonance, which cuts the high-inclination group. The low harmonics $z_k = k\,\nu_6 + \nu_{16}$ (k is a simple integer) also seem to be interesting, as they affect a large amount of real objects in the inner belt. For instance, as shown in Carruba et al. (2005), some of the V-type asteroids outside the Vesta family are former family members that migrated to their current positions via the interplay of the Yarkovsky effect and non-linear SRs and MMRs. In Section 5, we analyse the importance of each resonance using the numerical simulations of its effects on test particles.

5 AVERAGED DYNAMICAL MAPS

Although the dynamical maps analysed in Section 3 reveal the main features of the dynamics in the region under study, they suffer limitations coming from the use of a grid of osculating orbital elements. This does not allow us, for example, to superpose over this grid the position of real asteroids. Then, in order to analyse the distribution of real objects in the region under study, we need to introduce some proper elements. We have chosen the averaged orbital elements,

Table 2. The main non-linear SRs present in the low-inclination inner belt. The linear resonances (of first order) are as follows: (i) g-type with a generic argument $\nu_i = g - g_i$, when formed by a combination of the proper frequency of perihelion g and the fundamental frequencies of the precession of the planet perihelia, from Mars ($i = 4$) to Uranus ($i = 7$); (ii) s-type with a generic argument $\nu_{1i} = s - s_i$, where s and s_i are the proper frequency of node s and the fundamental frequencies of the planet nodes precession, s_i.

Group	Non-linear SR	Description
Low inclinations		
g-1	$2\,\nu_6 - \nu_5$	g-type
	$2\,\nu_6 - \nu_7$	resonances of perihelia
g-2	$3\,\nu_6 - \nu_5$	
	$3\,\nu_6 - \nu_7$	
s-1	$\nu_{16} - \nu_6 + \nu_5$	s-type
	$\nu_{16} - \nu_6 + \nu_7$	resonances of nodes
	$2\,\nu_{16} - \nu_{17}$	
s-2	$2\,\nu_{16} - \nu_6 + \nu_5$	
	$2\,\nu_{16} - \nu_6 + \nu_7$	
	$3\,\nu_{16} - \nu_{17}$	
gs-0-1	$2\,\nu_{16} + \nu_5$	gs-type
	$2\,\nu_{16} + \nu_7$	mixed resonances
gs-0-2	$3\,\nu_{16} + \nu_5$	
	$3\,\nu_{16} + \nu_7$	
gs-1	$2\,\nu_6 - \nu_5 - \nu_{16}$	
	$2\,\nu_6 - \nu_7 - \nu_{16}$	
	$\nu_6 - 2\,\nu_{16} + \nu_{17}$	
gs-2-1	$2\,\nu_6 + \nu_{16}$	
	$\nu_6 + \nu_5 + \nu_{17}$	
	$\nu_6 + \nu_7 + \nu_{17}$	
gs-2-2	$3\,\nu_6 + \nu_{16}$	
	$2\,\nu_6 + \nu_5 + \nu_{17}$	
	$2\,\nu_6 + \nu_7 + \nu_{17}$	
...		
gs-2-6	$7\,\nu_6 + \nu_{16}$	
	$6\,\nu_6 + \nu_5 + \nu_{17}$	
	$6\,\nu_6 + \nu_7 + \nu_{17}$	

defined as the mean values of the smoothed time series resulting from the numerical integrations. The SAM algorithm applied to the time series of the smoothed orbital elements automatically yields the averaged values of the semimajor axis, eccentricity and inclination, corresponding to each initial condition on the grid of the osculating elements.

The averaged orbital elements obtained can be plotted on the (a, I) representative planes, which we refer to as 'averaged dynamical maps' (Michtchenko et al. 2002). In this way, the osculating initial conditions uniformly distributed on the rectangular grid are transformed by the SAM into maps of elements averaged over the time-span of 4.2 Myr. In other words, the averaged maps show the final (after 4.2 Myr of gravitational interactions with the Sun and five planets, from Mars to Neptune) distribution of the test particles, which were initially distributed over a perfectly uniform rectangular grid.

The main advantage of averaged dynamical maps is that proper elements of real asteroids can be now plotted over them. This is especially useful if we want to compare the distribution of real objects with respect to the web of resonances in the region under study. In the top panels of Figs 5–9, we present the averaged dynamical maps covering five eccentricity intervals, which represent the inner asteroid belt. Each map is analysed individually in the following subsections.

The construction of the averaged maps has been explained in detail in Michtchenko et al. (2002). Here, we only briefly introduce some basic concepts needed to understand the information provided by the maps. In the domains of quasi-regular motion, a small change in the initial conditions leads to small variations of the proper elements. Consequently, the averaged elements show continuous variation when the initial conditions are gradually changed. Therefore, the regions of quasi-regular motion are dominated by a smoothed distribution of points in the averaged map.

In the domains of chaotic motion, small changes in the initial parameters can produce a large variation of the proper elements. In this case, if the chosen time-span is large enough, the SAM method detects the dispersion of the averaged orbital elements, and the domains of irregular motion are dominated by an erratic scattering of the points. Finally, in the case of MMRs, the averaging makes all resonant particles appear along the libration centres, whereas the neighbourhood of the resonance appears to be empty.

Although many aspects of the averaged maps change as a function of the eccentricity, there are some general features that are common to all. The regions of regular motion appear as domains of light curves of points in Figs 5–9. The resonant test particles are distributed along the resonant libration centres, indicating the exact location of these resonances. They appear as vertical bands of different widths, depending on the strength of the resonance. The domains of strong instabilities appear as empty regions, if the escape times are comparable with the time of integrations ($\sim$4.2 Myr in our case). This is the case of the ν_6 SR, whose action removes all test particles from the central diagonal zones in all panels in Figs 5–9. If the escape times are longer than the time-span covered by the numerical simulations, the dynamical instabilities make the dispersion of the test particles visible as a sea of chaotic motion in Fig. 2. For instance, this is the case of the ν_{16} SR, located above the ν_6 resonance on the maps.

One important dynamical property reflected in the averaged maps is the occurrence of non-linear SRs in the asteroid belt. The features observed in the top panels of Figs 5–9 as narrow (black) stripes cutting the (a, I)-plane are groups of non-linear SRs. The main ones are labelled by the corresponding group number from Table 2. It should be noted that the SRs do not appear in the dynamical maps of Fig. 2, because the $\sim$4.2 Myr integration time is not long enough to detect the diffusive effects of the non-linear SRs. However, these resonances are visible on the averaged maps because of the effect of excitation of the asteroidal eccentricities and inclinations that is reflected in the averaged orbital elements. Thus, the averaged dynamical maps indicate the exact location of the SRs in the space of the averaged elements and allow the estimation of their widths.

In contrast to MMRs, which are easily identified as vertical lines on the averaged maps (as a consequence of the fact that, up to first order in masses, the semimajor oscillations have no secular terms), SRs (both linear and non-linear) usually have complicated three-dimensional structures in the proper (a, I)-subspace and are not easily represented in a plane. Moreover, the location and shape of the SRs change significantly for different values of proper eccentricity.

There are mainly two distinct methods to obtain a position of SRs on the representative planes. The first consists of isolating the real objects in the AstDyS archive, which are close to a given SR, and approximating their distribution on the (a, I)-plane by some analytical curve. The other method is based on the approach of Milani & Knežević (1994), which allows us to obtain analytically the proper asteroidal frequencies as functions of the proper

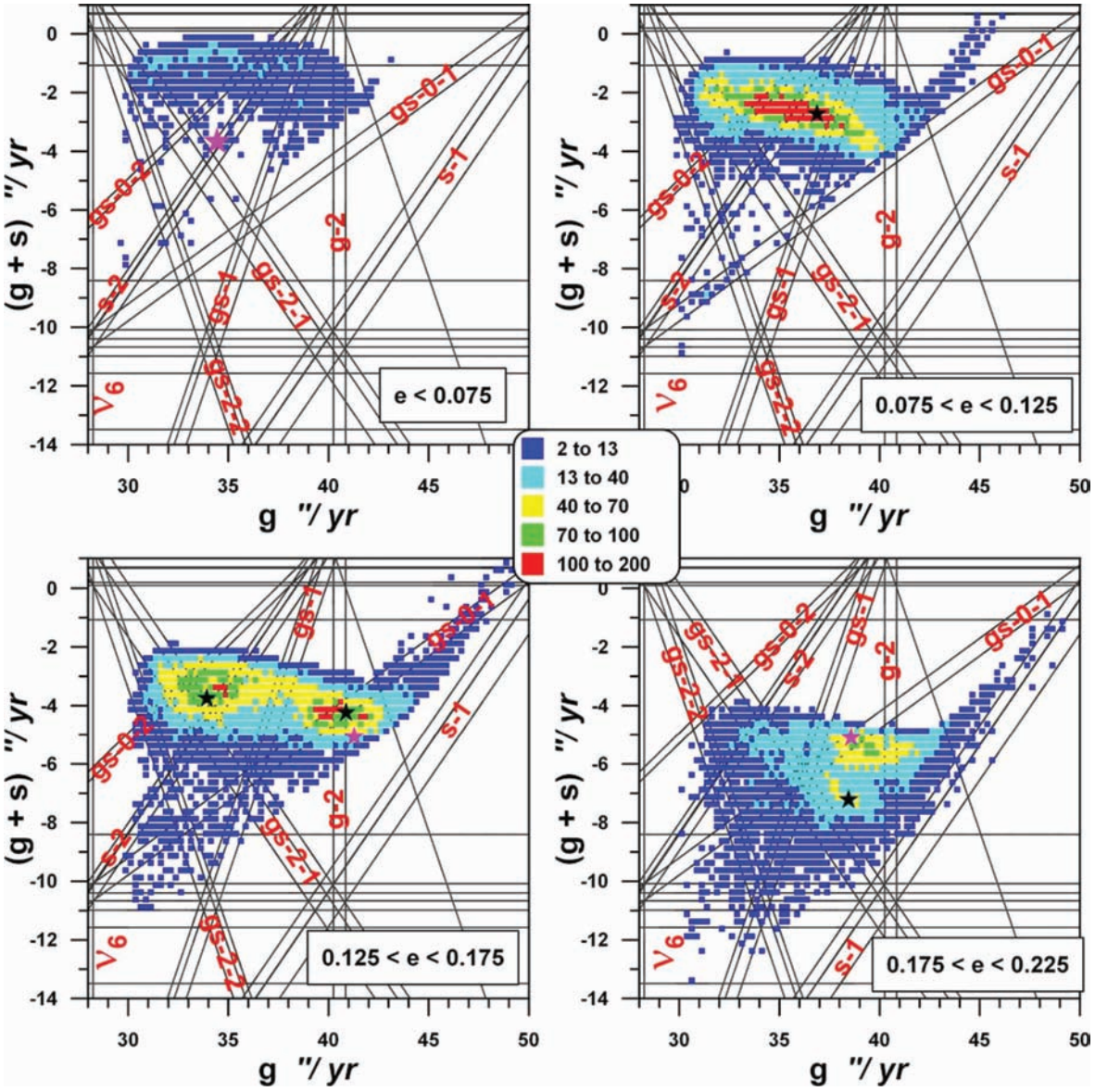

Figure 4. Density distribution of inner belt objects in the proper frequencies subspace $(g, g + s)$, with g and s being the asteroid frequency of perihelion and the frequency of node, respectively. The corresponding eccentricity interval is indicated at the bottom of each panel. The density (the number of asteroids inside a cell) is shown by different colours (see the legend box): blue corresponds to minimal values (<13) and red to maximal values (>100). The size of the cell is (0.25×0.25) arcsec yr^{-1}. The main linear and non-linear SRs in the region are shown by lines and identified by the group number from Table 2. Stars indicate the locations of the main objects of the detected families/groups.

semimajor axis, eccentricity and inclination, and, consequently, to calculate their resonant combinations with the fundamental planetary frequencies. In this work, we use the latter approach, keeping in mind that this method yields only approximated values of the proper frequencies.

In the following subsections, we investigate in detail the asteroid distribution in each eccentricity interval and its correlation with the dynamics in this region.

5.1 Very-low-eccentricity region (230 Athamantis)

The averaged map and the actual population with the proper eccentricities $e < 0.075$ are shown in Fig. 5. The domain under study is limited to low inclinations, below 18°. There are no known families in this region and we used the initial elements of the asteroid 230 Athamantis to construct the dynamical and averaged maps shown in Figs 2 and 5. 230 Athamantis has a magnitude of 7.3 and its proper elements are $a = 2.38$ au, $e = 0.043$ and $I = 10\overset{\circ}{.}2$. The location of this object on the averaged map is shown by a red star.

The bottom panel in Fig. 5 shows a distribution of the actual objects with proper eccentricities smaller than 0.075. Their total amount in the AstDyS archive is around 3000. The MMRs and SRs, whose effects are present in the averaged dynamical map, are sketched in the bottom panel. It is easy to distinguish the MMRs, which appear as vertical lines and are labelled by the corresponding group number from Table 1. The SRs are indicated by the corresponding group number from Table 2.

Not all MMRs and SRs present in Fig. 4 are actually important in the region of very low eccentricities. When the excitation as a result of resonances is small over 4.2 Myr, their effects are not observed

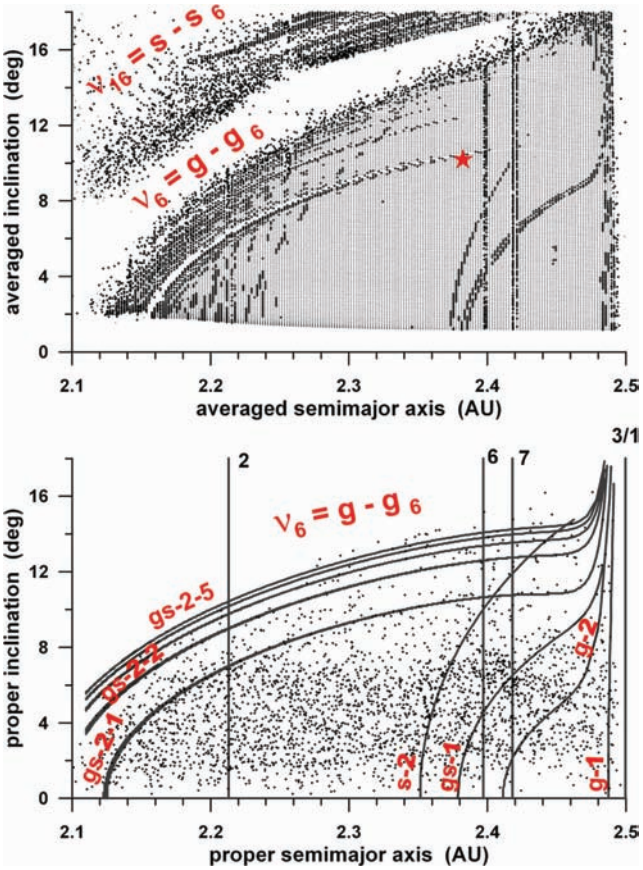

Figure 5. Top: averaged map around 230 Athamantis in the proper elements space limited to $I < 18^\circ$; 230 Athamantis is shown by a red star. Bottom: the main MMRs (vertical lines) and the strong linear and non-linear SRs in the region. The resonances are identified by the group number from Tables 1 and 2. The dots are proper elements of the objects within the corresponding eccentricity interval from the AstDyS catalogue.

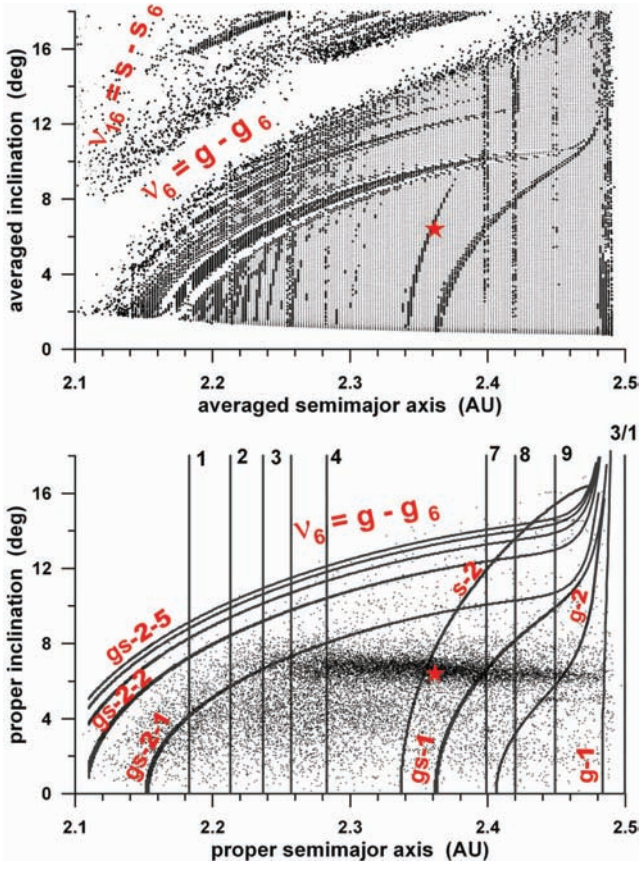

Figure 6. Same as in Fig. 5, except around 4 Vesta, shown by a red star on both panels. The Vesta family can be easily identified on the bottom panel as a huge concentration of objects around the red star.

on the averaged maps. Among the MMRs, only those that compose groups 6 and 7 are visible, for instance, the 1A/2M MMR with Mars and the first-order three-body 4J : −2S : −1A MMR, belonging to groups 6 and 7, respectively.

The non-linear SRs, which belong to groups g-2, s-2 and gs-1 in Table 2, may be observed on the right-hand side of the low-eccentricity domain in Fig. 5. They overlap with the MMR bands 6 and 7, producing a slightly enhanced concentration of objects in the overlapping region. It is worth noting that, because the strength of both MMRs and SRs is weak at very low eccentricities, only 1 per cent of the actual population shows signs of chaotic behaviour (see also Fig. 3). In the sample of test particles with initial conditions distributed in the rectangular grid in the ranges $2.1 \leq a \leq 2.5$ au and $0 \leq I \leq 18^\circ$, around a half show regular motion.

The bundle formed by the harmonics $k\,\nu_6 + \nu_{16} (k = 2, 3, \ldots)$, which belong to groups gs-2-1, gs-2-2, ..., converges to the linear ν_6 resonance and is clearly responsible for the upper boundary of the low-inclination asteroidal population. The puzzling decrease of the asteroidal density above $I = 8^\circ$, observed in the top-left panel of Fig. 1, even in the domains of apparently regular motion, may be explained by the very long acting dynamical effects of this bundle (much longer than the time-span of 4.2 Myr used in the construction of the maps). However, additional investigations should be carried out to provide more evidence in support of this conjecture.

Finally, on the right-hand side of the low-eccentricity domain, the most strong non-linear resonance is $2\,\nu_6 - \nu_5$ of order 3 from group g-1 in Table 2. The joint action of this SR and the 3J/1A MMR defines the limits of the actual objects in this part of the plane.

The loci of non-linear resonances depend strongly on eccentricities and vary inside each eccentricity interval under study. Moreover, as we use an analytical approach, which yields only approximated values of the proper frequencies (Milani & Knežević 1990), their determination is inaccurate. A correct estimation of the asteroidal distribution with respect to SRs can be made in the top-left panel of Fig. 4, where the density of objects with proper eccentricities $e < 0.075$ is shown in the proper frequencies subspace $(g, g + s)$. The previously detected low density of real objects on nearly circular orbits and the absence of the clusters observed in the proper elements space (see Fig. 1) are also observed in the frequency space.

The main linear and non-linear SRs in the region around 230 Athamantis are sketched and identified by the group number from Table 2. The very-low-eccentricity population forms a compact group in the frequency space, with a slight dispersion of the objects along the bands of the SRs. In particular, 230 Athamantis itself (magenta star) seems to evolve inside the s-2 group of SRs.

5.2 Low-eccentricity region (4 Vesta)

The region around 4 Vesta is defined by eccentricities in the range $0.075 \leq e < 0.125$ and is shown in Fig. 6. This region is probably the most studied in the inner belt, because of the presence of the well-known large family associated with 4 Vesta. The peculiar

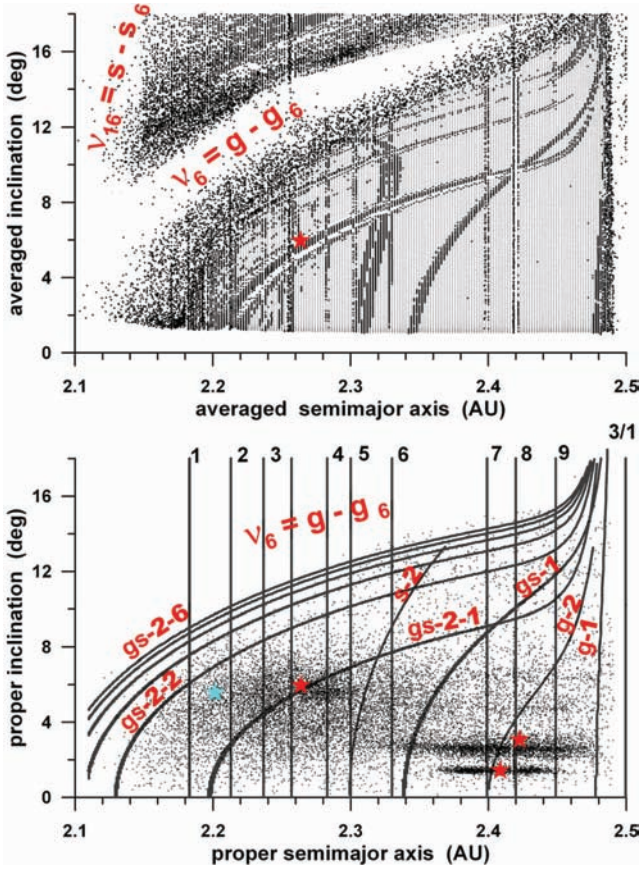

Figure 7. Same as in Fig. 5, except around 298 Baptistina, shown by a red star on both panels. The classical Massalia and Nysa families are easily identified on the bottom panel. The location of 8 Flora is shown by a cyan star.

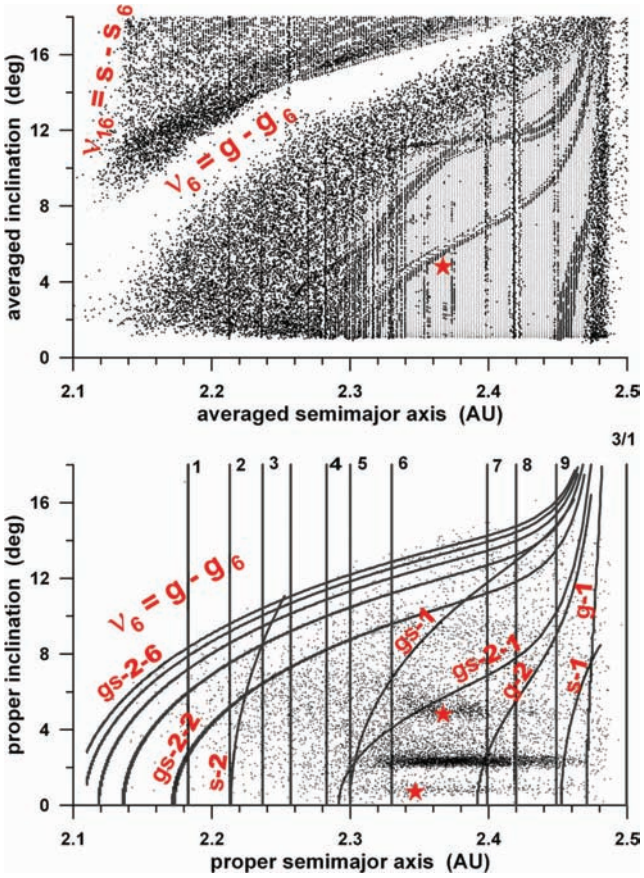

Figure 8. Same as in Fig. 5, except around 163 Erigone, shown by a red star on both panels. The main bulk of objects in the bottom panel is part of the Nysa family, while the Erigone family and the 27 Euterpe low-inclination group are not dense.

V-type (basaltic) asteroid 4 Vesta has a magnitude of 3.3 and its proper elements are $a = 2.36$ au, $e = 0.0988$ and $I = 6.^{\circ}4$. The location of 4 Vesta in both panels of Fig. 6 is shown by a red star and the associated dynamical family is clearly identified in the bottom panel. The total number of objects with proper eccentricities in the range $0.075 \leq e < 0.125$ is around 16 500.

The main structure of the dynamical portrait in this region is similar to that in Fig. 5. The ν_6 and ν_{16} SRs, as well as the MMRs, do not change their location, but just enhance their width. In contrast, the position of the non-linear SRs is clearly shifted on the (a, I)-plane, indicating their strong dependence on proper eccentricities. The bundle of the harmonics $k\,\nu_6 + \nu_{16} (k = 2, 3, \ldots)$ is descending in the direction of lower inclinations, while the s- and g- groups are moving towards smaller semimajor axes.

The large Vesta family is located in the central part of the region under study. Its boundaries seem to be defined by the resonance $2\nu_6 + \nu_{16}$ from the group gs-2-1, together with the 7J/2A MMR (left border), and the third-order $2\nu_6 - \nu_5$ SR from group g-1 (right border). The Vesta family interacts with the groups of MMRs from 4 to 9; in particular, a significant diffusion of its members is caused by the 1M/2A MMR (Carruba & Michtchenko 2009). Among the three-body resonances, 5J : −4S : −1A and 4J:-2S: − 1A also play a significant role in the dispersion of the family members.

The density distribution of the objects around 4 Vesta with respect to the SRs is shown in Fig. 4 (top-right). The role of the SRs in the dynamics of the members of the Vesta family is generally much slower, far more time being necessary to introduce significant effects, when compared to those as a result of the MMRs (Carruba et al. 2005). Four groups of non-linear SRs (gs-0-2, gs-1, s-2 and gs-2-1) perturb family members and may be responsible for dispersion of the V-type objects in the inner part of the asteroidal belt. In particular, the effects produced by the s-type $(3\nu_{16} - \nu_{17})$ SR of order 4, from group s-2, have been studied in Carruba & Michtchenko (2009). The dispersion of the objects in the direction of lower $(g + s)$ values (corresponding to higher inclinations) is enhanced, mainly along the gs-0-1 group of SR, which forms the natural right border of the region.

The population of the Vesta region is about 5.5 times larger than that in the previous interval, and reaches about 16 500 objects. As shown in Section 6, the sudden increase in the population is because of the existence of the large Vesta family, rich in small-sized objects. Among the total number of actual objects within this eccentricity interval, 3 per cent are involved in chaotic motion, related mainly to the action of MMRs. Among the test particles distributed in the rectangular grid in the ranges $2.1 \leq a \leq 2.5$ au and $0 \leq I \leq 18^{\circ}$, around 45 per cent show regular motion.

5.3 Moderate-eccentricity region (298 Baptistina)

The averaged map and the actual population in the eccentricity range $0.125 \leq e < 0.175$ are shown in Fig. 7. There are three known groups of asteroids in this region, associated with 20 Massalia, 44 Nysa and 298 Baptistina. We used the initial elements of 298 Baptistina to construct the dynamical and averaged maps. 298 Baptistina has

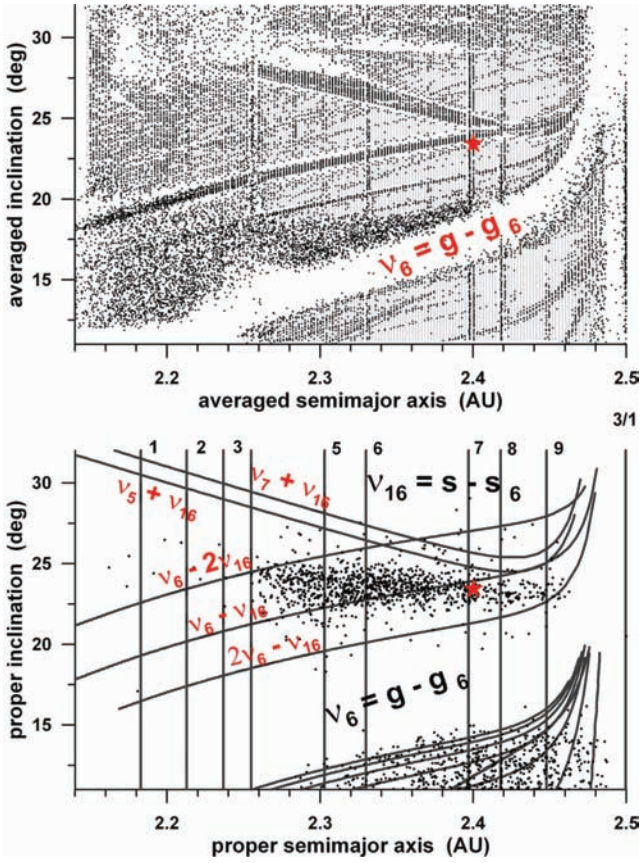

Figure 9. Top: averaged map around 25 Phocaea in the proper elements space bounded by $11^\circ < I < 32^\circ$. Bottom: the main MMRs (see Table 1) and the strong linear and non-linear SRs in the region. The Phocaea group of the highly inclined objects is superposed.

a magnitude of 11.1 and its proper elements are $a = 2.26$ au, $e = 0.148$ and $I = 5\overset{\circ}{.}96$. The total amount of objects with proper eccentricities in the range $0.125 \leq e < 0.175$ is around 18 500.

Although the main non-linear SRs now cover a central zone of the representative plane, the changes in the chaoticity of the region are relatively small. Only 12 per cent of the actual objects inside this eccentricity interval are involved in chaotic motion (see Fig. 3). From the sample of the test particles in this eccentricity interval and with the initial condition distributed on the rectangular grid in the ranges $2.1 \leq a \leq 2.5$ au and $0 \leq I \leq 18^\circ$, around 40 per cent show regular motions.

From the detected asteroidal groups present in the region, those associated with Massalia and Nysa are large, both having a typical asteroidal family shape, characterized by a significant dispersion along the semimajor axis and aligned along an almost constant inclination, around $I = 1\overset{\circ}{.}4$ and $I = 2\overset{\circ}{.}6$, respectively. The Massalia family is smaller, but has the highest density in the whole inner belt, indicating that this may be a relatively young family. Estimates of its age based on a Monte Carlo simulation of the Yarkovsky and YORP diffusion of family members on the semimajor axis gives a family age of 190^{+40}_{-20} Myr (Vokrouhlický et al. 2006).

The structure of the Nysa family is more complicated; it seems to be composed of three different subclusters, related to 878 Mildred, 135 Hertha and 2007 McCuskey (the former Polana family of Cellino et al. 2001). Of these clusters, the first two are associated with the S- and X-type, while the third is related to the C-type (Mothé-Diniz, Roig & Carvano 2005). At present, it is not clear if the Hertha and Mildred clusters should be considered as two families originated from different breakup events, or one single family formed by the disruption of a differentiated body. The location of 44 Nysa far from the epicentre of the associated group only emphasizes the uncertainty about the origin of the associated agglomeration.

From a dynamial point of view, the Massalia and Nysa groups are located at the relatively 'quiet' region characterized by the absence of activity of strong MMRs and SRs. Both are crossed by the MMR bands from 7 to 9, with only the 1M/2A and $4J : -2S : -1A$ resonances showing some significant effects. The position of the two families in the frequency space with respect to the SRs is shown in Fig. 4 (bottom-left). The g-2 and g-0-1 groups of the non-linear SRs cut through the families and may be responsible for the dispersion of the objects in the region, particularly of 44 Nysa (magenta star) itself, which is clearly far from the centre of the associated family.

In contrast to other families of the region, the Baptistina group is located in the dynamically active region, where the MMR groups from 3 to 6 intersect the bands gs-2-1 and s-2 of the SRs (Fig. 7). The superposition of many, even weak, resonances may produce efficient mechanisms to disperse the population in the overlapping region. There are several signs that the objects from the left half-plane in Fig. 7 have experienced the effects of these mechanisms: (i) the enhancement of the background density (see Fig. 1); (ii) the elevated concentration of large asteroids, with $D > 10$ km (see Figs 2 and 11); (iii) the increased percentage of objects in chaotic orbits (see Fig. 3); (iv) the considerable dispersion in inclination and irregular shape of the Baptistina group, contrasting with the shapes of the other families (see Fig. 7). A detailed study of this group is beyond the scope of this paper, and will be addressed in a paper already in preparation.

Finally, as seen in Fig. 7, the g-1 group of SRs forms a natural right border of the moderate-eccentricity region. Practically all objects existing beyond this border are strongly chaotic, which is confirmed by the distribution of the unstable orbits shown in Fig. 3.

5.4 High-eccentricity region (163 Erigone)

Fig. 8 shows the averaged map (top panel) and the actual population (bottom panel) corresponding to the eccentricity range $0.175 \leq e < 0.225$. There is a small asteroid group associated with 163 Erigone, the orbital elements of which are used to construct the maps. 163 Erigone has a magnitude of 9.1 and its proper elements are $a = 2.37$ au, $e = 0.21$ and $I = 4\overset{\circ}{.}8$. The total number of objects with proper eccentricities in the range $0.175 \leq e < 0.225$ is around 10 500.

The most important feature observed in both panels of Fig. 8 is a significant degradation of the stability of asteroidal motion in this eccentricity interval. Indeed, about 40 per cent of the real objects inside this region show chaotic behaviour; from the sample of the test particles with the initial condition distributed on the rectangular grid in the ranges $2.1 \leq a \leq 2.5$ au and $0 \leq I \leq 18^\circ$, only 25 per cent show regular motions. This rapid degradation occurs as a result of the devastating actions of the overlapping resonances, increasing in width and strength with increasing eccentricities (also observed in Fig. 2).

The left half-plane of the high-eccentricity region is totally dominated by chaotic orbits, as seen on the averaged map in Fig. 8. Despite the instabilities in asteroidal motion, this part is still populated by a significant amount of objects, with density indices comparable with those of the nearly circular orbits. The gs-1 group of SRs

separates the chaotic region from the region of quasi-regular motion, where the asteroid families are concentrated. These are the 44 Nysa family (the members with $e > 0.175$), the 163 Erigone family and an additional small group of the low-inclination asteroids, centred around 27 Euterpe.

The presence of the Nysa family is responsible for the relatively large number of objects at high eccentricities. As seen later, in this region the number of large asteroids, with $D > 100$ km, reaches the value of 6. It is curious that all large bodies, with the exception of 27 Euterpe, seem to be involved in some type of resonance, indicating the action of diffusion mechanisms.

The distribution of the high-eccentricity objects in the frequency space is shown in Fig. 4 (bottom-right). The intersection of the several bands of SRs, observable at the central part of the panel, is clearly one of the causes of the degradation of stability in this part of the belt. The most effective band in dispersion is gs-2-1, which is characterized by the enhanced density of objects (cyan cells). Finally, the physical right-hand border of the region is delimited by the g-1 group, and many objects are found evolving in the $(2\nu_6 - \nu_5)$ SR, belonging to this group.

5.5 Objects on eccentric and highly inclined orbits (25 Phocaea)

With increasing eccentricities, the low-inclination asteroid population is rapidly reduced. The amount of objects with proper eccentricities $e > 0.225$ in the AstDyS catalogue is around 2000; at $e = 0.30$, the low-inclination region is practically empty. Of these, only 10 per cent have Lyapunov times larger than 25 000 yr (i.e. stable at least over short time-spans).

Fig. 9 shows the averaged map (top panel) and the actual population (bottom panel) corresponding to the range with eccentricities $e \geq 0.18$. The domain under study is now limited to moderate and high inclinations, in the range $11^\circ \leq I \leq 32^\circ$. This region, located above the ν_6 SR on the (a, I)-plane, has received little attention, and many issues concerning the origin and stability of the objects in this region are still open for discussion.

We know that there exists a very special population and the number of its members in the AstDyS catalogue is small, around 1400 objects. The most interesting fact, from a dynamical point of view, is the existence of the asteroidal group associated with 25 Phocaea. Beside the Phocaea group, there are also two other small groups, associated with 1660 Wood and 5247 Krylov (Knežević & Milani 2003; Gil-Hutton 2006).

Delimited by the ν_6 (lower boundary) and ν_{16} (upper boundary) SRs, the region seems to be an island of stability, but with a complicated internal structure. The strong second- and third-order non-linear SRs cut the region: the main SR is the $\nu_6 - \nu_{16}$ SR and part of the Phocaea group is captured in this resonance. This resonance is accompanied by two close harmonics of order 3: $2\nu_6 - \nu_{16}$ and $\nu_6 - 2\nu_{16}$, the latter with a significant number of captured objects.

6 SIZE DISTRIBUTION OF INNER BELT OBJECTS

The size distribution of asteroids is a complex issue. This is because the actual size of an asteroid is a function of its magnitude (which is always known) and its albedo (which is unknown for the majority of objects). The relatively small amount of objects (2228) with measured albedos are catalogued in the IRAS data base (Tedesco et al. 2002).

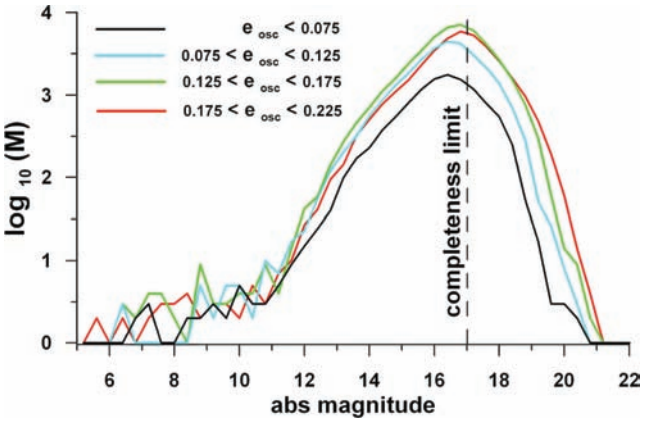

Figure 10. Number of objects (M) as a function of the absolute magnitude (mag), in logarithmic scale. M was calculated in a cell defined as mag ± 0.2, for the objects from the Bowell catalogue. The different colours show different intervals of the asteroid eccentricity in the osculating space.

In a first approach, the sizes of objects can be roughly substituted by their absolute magnitudes. Fig. 10 shows a histogram of the absolute magnitudes of the inner belt objects extracted from the Bowell catalogue; the different colours correspond to the previously defined eccentricity intervals. The non-cumulative frequency of the objects was calculated in cells with magnitude width equal to 0.4. The completeness of the sample is clearly limited to magnitudes less than $\sim$17.

The frequency of the objects with an absolute magnitude less than 12 seems to be randomly distributed in all eccentricity intervals, but the sample seems to be statistically insignificant and we cannot derive any reliable conclusions. The number of smaller objects is clearly increased in the eccentricity intervals that contain large families. Thus, the high values of density index observed in Fig. 1 are directly correlated with the presence of asteroidal families.

To refine our analysis on the size distribution, we transform the absolute magnitudes in the actual size, for objects whose surface compositions are known from either spectroscopic or photometric observations (gathered at http://www.psi.edu/pds/asteroid). Indeed, the albedo is related to the surface composition of an asteroid, which, in principle, should be associated with its taxonomic classification. However, it is important to emphasize that this is a very naïve approach, as the same albedo has been observed in different taxonomic types, linked to completely different mineralogies.

Keeping in mind the above limitations, we start by defining four size ranges: greater than 100 km, between 50 and 100 km, between 10 and 50 km, and smaller than 10 km. It is worth noting that, for magnitudes greater or equal to 13, the assumed value of albedo does not change the interval to which an asteroid belongs. Moreover, this is the magnitude of the majority of asteroids, for which we have no observed albedo. Therefore, in what follows, all objects with a magnitude greater or equal to 13 are considered to have a size smaller than 10 km. For asteroids with a magnitude smaller than 13, we use the observed albedo, when available in the IRAS catalogue, and, for the rest of the objects, an averaged value of albedo of 0.23. This averaged value has been obtained in the range of the observed albedos, between 0.06 of C-type objects, and 0.40, related to the basaltic composition of Vesta and V-type objects.

The size distribution of the inner belt objects in the proper elements space is shown in Fig. 11. The different colours represent the different intervals of the asteroid size: the large objects (with $D \geq 100.0$) are shown by red crosses, the intermediate

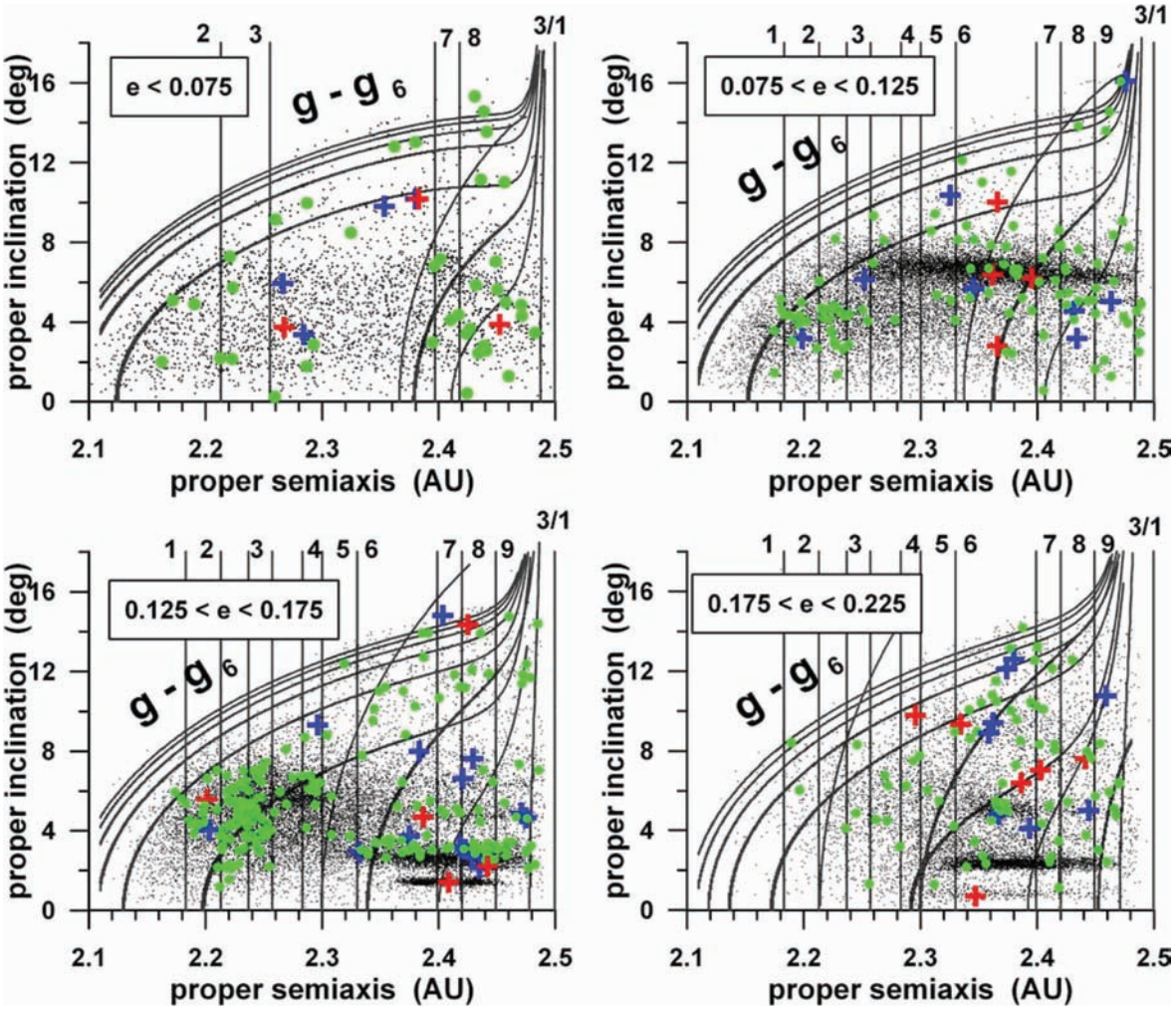

Figure 11. Size distribution of the known objects in the proper elements space. Black dots represent the main bulk of the inner belt population. The groups of MMRs and non-linear SRs in the region are shown. The population is shown by red crosses (objects with a diameter greater than 100 km), blue crosses ($50 < D \leq 100$ km), green full circles ($10 < D \leq 50$ km) and black dots ($D < 10$ km).

objects (with diameters between 10 and 100) by blue and green symbols, and the smaller objects (with $D < 10$) by black dots. There are three large ($D > 100$ km) asteroids on nearly circular orbits: 11 Parthenope, 40 Harmonia and 230 Athamantis. In the range $0.075 < e < 0.125$, there are four large objects (4 Vesta, 30 Urania, 51 Nemausa and 63 Ausonia), while at moderate eccentricities the number increases to five (6 Hebe, 8 Flora, 9 Metis, 19 Fortuna and 20 Massalia). Finally, at high eccentricity, there are six objects: 7 Iris, 12 Victoria, 18 Melpomene, 27 Euterpe, 42 Isis and 105 Artemis. It is worth noting that in the sample of 19 large asteroids in the inner belt, the majority belong to the taxonomic S class, with exception of the V-type 4 Vesta and three C-type objects, 19 Fortuna, 51 Nemausa and 105 Artemis, with proper elements $a = 2.442$ au, $e = 0.1345$, $I = 2\overset{\circ}{.}2$, $a = 2.365$ au, $e = 0.114$, $I = 10\overset{\circ}{.}0$ and $a = 2.37$ au, $e = 0.205$, $I = 21\overset{\circ}{.}76$, respectively.

A notable feature observed in Fig. 11 is the relation between the locations of the large objects (red and blue crosses) and of the MMRs and SRs. Indeed, almost all large bodies, with $D > 50$ km, are located close to characteristic curves on the representative plane, especially those at high eccentricities and inclinations. From our previous investigations (Carruba et al. 2005), we know that capture in MMRs and SRs is a process that strongly depends on the rate of the Yarkovsky diffusion of asteroids, which is a function of the asteroid's diameter. We expect that only large bodies, whose response to the Yarkovsky effect is weak, will perform long-lasting drifts along the SRs, before reaching the regions of large-scale instabilities. To confirm this scenario requires additional detailed investigations.

7 TAXONOMIC DISTRIBUTION OF INNER BELT OBJECTS

To verify how the density distribution of real asteroids correlates with their taxonomic classes, we have analysed a sample of asteroids from the fourth release of the Sloan Digital Survey Moving Object Catalogue (Juric et al. 2007). The objects were classified into broad taxonomic classes using a new taxonomic scheme (Lazzaro et al. 2009), which was designed to be compatible with previous taxonomies based on low-dispersion spectra (Bus & Binzel 2002) and spectrophotometry (Tholen & Barucci 1989).

In essentially all taxonomic schemes, most asteroids fall into three broad classes. The S class is characterized by the presence of a broad 1-μm band, as a result of crystal-field transitions of olivine and/or pyroxene. The C and X classes are both mostly featureless

in the visible and differ mainly by the spectral gradient, which is neutral to slightly negative for C-class asteroids and moderately positive for asteroids belonging to the X class. For all three classes, the associations with mineralogy are ambiguous. S-class asteroids may have either mineralogies compatible with ordinary chondrites or some stony achondrites, while X and C classes may harbour mineralogies compatible with carbonaceous chondrites, enstatite chondrites, enstatite achondrites or ferrous meteorites (Tholen & Barucci 1989; Britt et al. 1992; Carvano, Mothé-Diniz & Lazzaro 2003; Lazzaro et al. 2009).

Here, we analyse the distribution of asteroids belonging to the two distinct classes: S and C/X. The latter represents a combination of the C and X classes. This is possible because both represent broadly overlapping mineralogies, and also because the distinction between most of the spectral subtypes in these classes is arbitrary. Fig. 12 shows a density plot, similar to Fig. 1, of the subsample of S-class asteroids with known proper elements, in total 6238 individual objects. Fig. 13 shows a similar plot, for 3905 C/X-class asteroids. It should be noted that no attempt was made to perform bias correction.

Several notable characteristics of the distribution of the S and C/X asteroids can be observed in Figs 12 and 13. The S-type asteroids dominate at eccentricities <0.075 (top-left panel in Fig. 12). In the eccentricity range $0.075 \leq e < 0.125$ (top-right panel), the asymmetric structure of the density distribution observed in Fig. 1 seems to be composed only of S-class asteroids. However, there is evidence of some deficit of S-type asteroids at low inclinations and $a > 2.3$.

The S-type population is extended beyond $I > 8^\circ$, for all values of proper eccentricity. The evident increase of the density of S-type asteroids occurs at moderate eccentricities and is associated with the Nysa and Massalia families (bottom-left panel of Fig. 12). There is also a broad, ellipsoidal region of enhanced density of S-type asteroids, which is not clearly associated with any family; we have associated it with the Flora clan (Florczak et al. 1998). At high eccentricities (bottom-right panel), the observed overdensity of S-type objects corresponds to the Nysa family.

In contrast, the C/X-class asteroids are generally more sparsely distributed in the inner part of the main belt. This is particularly true for the nearly circular orbits, which are few and scattered (top-left panel in Fig. 13). They do not present an asymmetric increase in density at low eccentricities (bottom-right panel), but seem to be depleted in a broad region defined roughly within $2.3 \leq a \leq 2.4$ au and $4^\circ \leq I \leq 7^\circ$ on the representative plane; this region is associated with the Vesta family. The C/X-class objects also seem to be depleted at small inclinations and $a < 2.4$ au.

The third eccentricity interval within $0.125 \leq e < 0.175$ (bottom-left panel in Fig. 13) shows an increase in density in the regions corresponding to the families of Baptistina, Nysa and Massalia. The overdensity around Baptistina is two-peaked, with 298 Baptistina falling between the two peaks. There is also an overdensity of

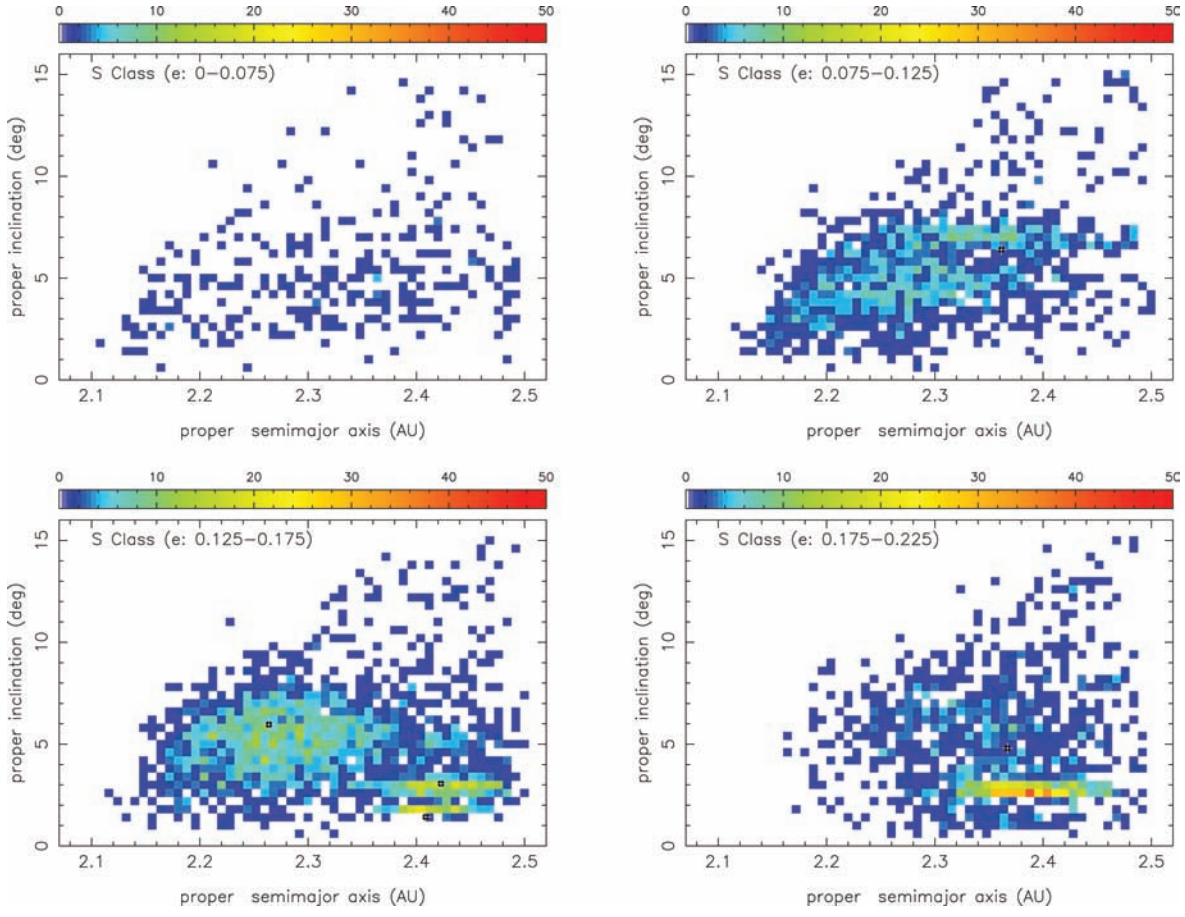

Figure 12. Density of S-type asteroids from the Sloan Digital Survey Moving Object Catalogue (Juric et al. 2007). Classification was carried out using a taxonomic scheme from Lazzaro et al. (2009). The eccentricity interval is indicated at the top of each panel. Symbols represent the largest nominal members of the Vesta, Baptistina, Nysa, Massalia and Erigone families.

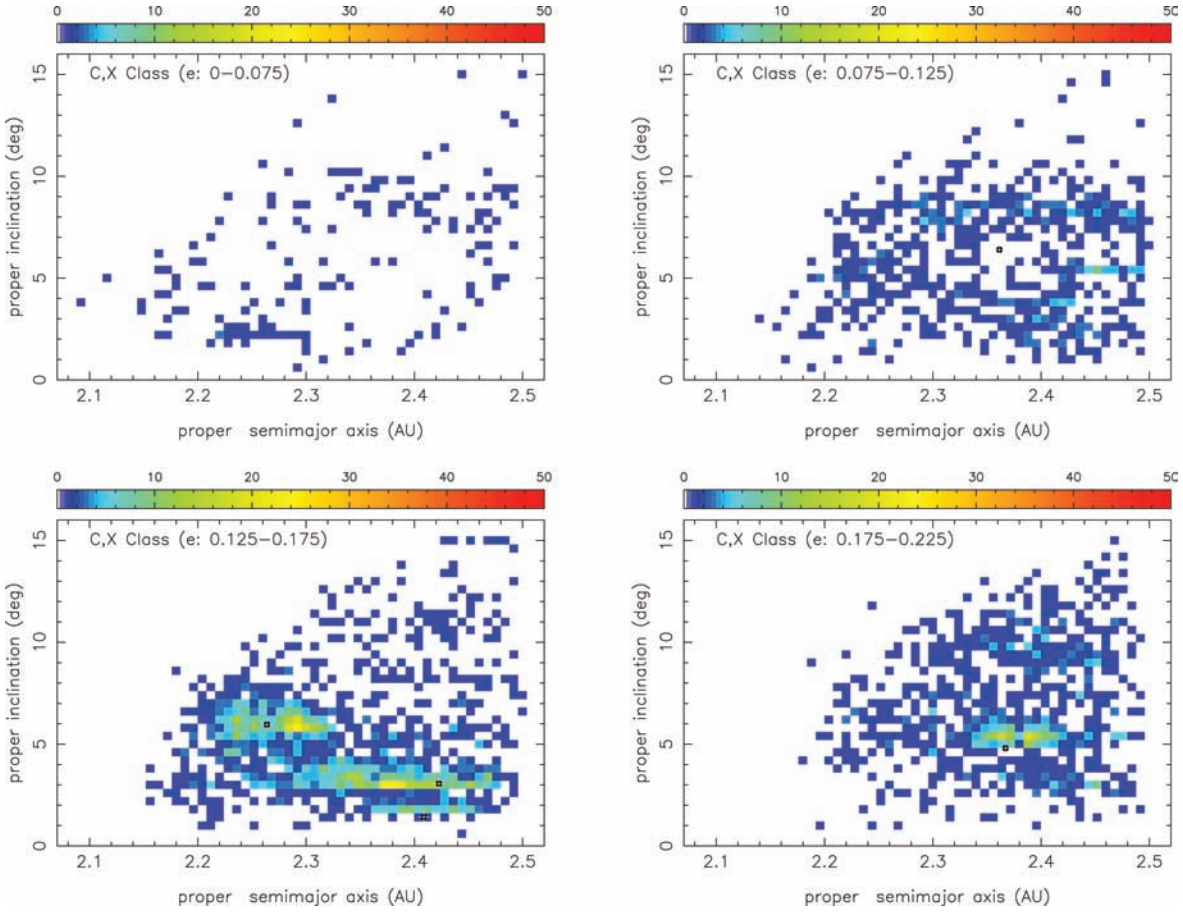

Figure 13. Same as in Fig. 12, for the taxonomic C/X class of asteroids.

C/X-type asteroids in the Nysa and Massalia family domains. For the Nysa family, the higher density region is shifted towards a lower semimajor axis with respect to 44 Nysa itself and to the overdensity observed for the S-type asteroids in this region. The overdensity in the Massalia region, however, shows no spread in inclination and seems to be strongly correlated with the overdensity observed for S-type asteroids around this family.

Finally, in the high-eccentricity region within $0.175 \leq e < 0.225$ (bottom-right panel), there is an overdensity in the region of the Erigone family, which is shifted with respect to 193 Erigone. In this region, the C/X-type asteroids seem also to be depleted at low inclinations.

8 SUMMARY

In this paper we have presented a dynamical portrait of the inner part of the asteroidal belt, confined in the semimajor axis interval from 2.1 to 2.5 au.

To construct it, we performed several steps, as follows.

(i) We plotted the density distribution of the asteroid population in the proper elements space and identified its features.

(ii) We identified asteroidal families in the region.

(iii) We carried out dynamical mapping of the representative planes in the $(a_{\rm osc}, I_{\rm osc})$-space.

(iv) We plotted the asteroid population in the proper frequencies space and detected the main MMRs and SRs acting in the region under study.

(v) We constructed the averaged maps and identified the dynamical mechanisms responsible for the actual shape of the asteroid distribution.

(vi) We examined possible interactions between actual objects and the web of resonances, as a source of diffusion of small bodies.

(vii) We studied the dynamical implications on the size and spectral distribution of real objects in the inner main belt.

The methods used in this work are mainly numerical. The analysis employs the SAM, which allows us to construct dynamical, averaged and frequency maps. The investigations have been carried out in both the proper elements and proper frequencies spaces. The three-dimensional elements space is represented by five subspaces on the proper (a, I)-planes, each characterized by different eccentricity intervals: nearly circular orbits ($e < 0.075$), low-eccentricity orbits ($0.075 < e \leq 0.125$), moderate-eccentricity orbits ($0.125 < e \leq 0.175$), high-eccentricity orbits ($0.175 < e \leq 0.225$) and very-high-eccentricity orbits ($e > 0.225$). The presentation of the proper frequencies is easier and requires only two subspaces, the $(n, g + s)$ and $(g, g + s)$ planes, where n, g and s are the asteroid mean motion, the frequency of perihelion and the frequency of node, respectively.

We characterized each plane in order to investigate the possible dynamical mechanisms that could provoke asteroidal diffusion and the observed peculiarities in the distribution of the population in the inner belt. In this way, we have identified the main MMRs and SRs as a possible source of excitation of asteroidal motion and chaotic drift of objects in the proper elements space. The dense web formed by MMRs and SRs is sketched and superposed on the asteroidal

distribution in both the proper elements and proper frequencies spaces. As the comparison is only possible in the proper space, the proper elements data base of Milani and Knežević is indispensable for this study.

The population of the inner belt is bounded by the linear ν_6 and ν_{16} SRs from the left-hand side and by the 3J/1A MMR with Jupiter from the right-hand side on the (a, I)-plane, in all eccentricity intervals. A major portion of objects is concentrated in the low-inclination region, which is delimited by the ν_6 SR, for all eccentricities. A significant high-inclination population exists only at high eccentricities and is confined to the region between the ν_6 and ν_{16} SRs. The origin of high-inclination objects is still uncertain, but it is probably connected to the web of resonances.

The presence of linear SRs (with the planets from Mars to Uranus), in the immediate proximity of the inner belt, generates a huge number of low-order non-linear resonances, which densely cover the region under study. Their effects are not as devastating as those of the linear resonances, but are still very important for the transport of objects and could explain many features seen in the asteroid distribution. Indeed, non-linear SRs, interacting with the Yarkovsky dissipation, excite the asteroidal eccentricities and inclination and provoke slow diffusion of objects in the high eccentricity and inclination regions. As a result of the Yarkovsky effect, their actions are size-dependent and this could explain the correlation between the distribution of large asteroids, with $D > 50$ km, and SRs seen in Fig. 11.

In contrast with SRs, the MMRs present in the inner belt are not very strong, despite the 3J/1A MMR with Jupiter, which creates a natural right-hand border of the inner belt. MMRs are weak because of large distances to the Jupiter–Saturn system, which is acting from the right-hand side, and the very small mass of Mars, which is acting from the left-hand side of the inner belt. Many objects are seen to be involved in the MMRs, mainly in the 7J/2A MMR with Jupiter and the 1A/2M MMR with Mars.

The representation of inner belt objects on the (a, I)-planes, constructed in the different eccentricity intervals, allows us to visualize clearly the asteroidal families present in this region. Almost all groups of objects appear as clusters expanded significantly in semimajor axes, but confined strongly in inclinations. This characteristic shape of a family is easily understood in the context of orbital dynamics, when, to change the plane of its orbits, the particle must gain several orders more kinetic energy than the quantity of energy necessary to change its semimajor axis and eccentricity. In addition, the Yarkovsky acceleration, acting along the asteroidal semimajor axes, enhances this effect.

We confirm the existence of the well-known large families in low and moderate eccentricities, which are associated with 4 Vesta, 20 Massalia and 44 Nysa. We also identify the dynamical features (MMRs and SRs) that interact with these families and may provoke a slow diffusion of their members out of the family regions. We suggest that specific investigations, performed in the domain of each family, could confirm this dispersion scenario and provide an estimation of the lifetime of the family, as has been done for the neighbourhood of the Vesta family (Carruba et al. 2005; Carruba, Michtchenko & Lazzaro 2007).

The small agglomerations, characterized by the irregular distribution of their members, need to be examined carefully. To assess the nature of these groups, we need additional information on the surface composition of a significant number of their members. This is the case of the 163 Erigone group. The analysis of the taxonomic distribution, showing clearly around the C-type 163 Erigone the concentration of objects of the same taxonomy, confirms this group as a dynamical family originated by the same parent body. The same approach can be applied to the concentration of objects at very small inclinations around the large object 27 Euterpe, which belongs to the taxonomic S class; the absence of C/X-class objects in this region enforces the hypothesis about the collisional origin of this group. In this case, the size distribution of the objects is indicative: the presence of one large object, 27 Euterpe, at the low-inclination region, allows us to detect, using the hierarchical clustering method (HCM), a new cluster of objects associated with it.

A curious case is that of the small Baptistina group, whose shape clearly contrasts with those of other families. When we apply the mineralogical approach to identify a family, we are using the concept of homogeneity in the taxonomy distribution of the members. This means that the associated mineralogy must be consistent with the breakup of a unique body. In the case of the Baptistina cluster, this approach fails. We can clearly observe, around 298 Baptistina, the simultaneous enhancement of the density of the two distinct taxonomy classes, S and C/X. The possible explanations are as follows. (i) There is no family, but only an accumulation of objects of distinct classes at the intersection of the two strong bands of SRs and the two bands of MMR. (ii) We really detect the family, whose epicentre is in the complicated region of overlapping of several MMRs and SRs; because of their long-lasting action, the resulting family has been dispersed beyond recognition. In any case, additional observations are required to verify the authenticity of each of these hypotheses.

In addition, there are other non-conclusive facts concerning the asteroidal distribution in the inner belt, one of which is the absence of clusters of objects in near-circular orbits. The good news is that the absence of families at very low eccentricities allows us to estimate the density, size and taxonomy distribution of background objects in the inner belt. In contrast with the domain of nearly circular orbits, the high-eccentricity region is significantly populated by large objects. This distribution suggests that the population of the inner belt may have experienced long-lasting chaotic diffusions in the direction of high eccentricities, as a result of some dynamical mechanisms. There is one further fact concerning the distribution of chaotic objects from the AstDyS catalogue, with Lyapunov times $<25\,000$; for some reason, they form high-density regions in the domains of the Nysa and Erigone families.

The origin of the high-inclined population is also an open issue, although there is some evidence that it could have been formed as a deposit of diffusing chaotic objects inside stable islands (Carruba 2009). There are similar islands at low eccentricities, but all of these are empty. This issue could be related to the concept of angular momentum, which is lost by the massless objects during strong chaotic interactions and/or close approaches with the planets.

The taxonomic distribution of inner belt objects is strongly correlated with the distribution of their density indices. In particular, the distribution of S-type objects mimics the density distribution of the whole population, except in the two regions associated with the Vesta (V class) and Erigone (C class) families. It is worth noting that the majority of large objects, with $D > 100$ km, belong to the taxonomic S class. In general, S-type asteroids are evenly distributed in the inner main belt, showing broad concentrations in the intermediate eccentricity intervals that are not readily associated with dynamical families. However, they avoid the region of lower inclinations and $a > 2.3$ au for eccentricities $0.075 \leq e \leq 0.125$. For C/X-type asteroids, the only increases in density occur around dynamical families, with background objects depleted for $e < 0.07$ and at lower inclinations (especially for $a < 2.3$ au). Although it has been known for some time that S-type asteroids are more numerous

at the inner part of the main belt, these fine-grained differences in the distribution of background objects (i.e. objects not associated with dynamical families) have not previously been discussed in the literature.

ACKNOWLEDGMENTS

This research has been supported by the Brazilian National Research Council (CNPq), the São Paulo State Science Foundation (FAPESP) and the Rio de Janeiro State Science Foundation (FAPERJ). The authors gratefully acknowledge the support of the Computation Center of the University of São Paulo (LCCA-USP) and of the Astronomy Department of the IAG–USP for the use of their facilities.

REFERENCES

Bowell E., Muinonen K., Wasserman L. H., 1994, in Milani A., di Martino M., Cellino A., eds, Asteroid, Comets and Meteorids III. Kluwer, Dordrecht, p. 477
Britt D. T., Tholen D. J., Bell J. F., Pieters C. M., 1992, Icarus, 99, 153
Burbine T. H., Binzel R. P., 2002, Icarus, 159, 468
Bus S. J., Binzel R. P., 2002, Icarus, 158, 146
Carruba V., 2009, MNRAS, 398, 1512
Carruba V., Michtchenko T., 2007, A&A, 475, 1145
Carruba V., Michtchenko T., 2009, A&A, 493, 267
Carruba V., Michtchenko T., Roig F., Ferraz-Mello S., Nesvornỳ D., 2005, A&A, 441, 819
Carruba V., Michtchenko T., Lazzaro D., 2007, A&A, 473, 967
Carvano J. M., Mothé-Diniz T., Lazzaro D., 2003, Icarus, 161, 356
Cellino A., Zappala V., Doressoundiram A., di Martino M., Bendjoya Ph., Dotto E., Migliorini F., 2001, Icarus, 152, 225
Farinella P., Vokrouhlický D., 1999, Sci, 283, 1507
Ferraz-Mello S., 2007, Canonical Perturbation Theories, Degenerate Systems and Resonances. Springer, New York, p. 88
Florczak M., Barucci M. A., Doressoundiram A., Lazzaro D., Angeli C. A., Dotto E., 1998, Icarus, 133, 233
Gil-Hutton R., 2006, Icarus, 183, 93
Juric M., Ivezic Z., Lupton R., SDSS Collaboration, 2007, Bull. Am. Astron. Soc., 39, 828
Knežević Z., Milani A., 1994, in Milani A., Di Martino M., Cellino A., eds, Asteroids, Comets, Meteors. Kluwer, Dordrecht, p. 143
Knežević Z., Milani A., 2000, Celest. Mech. Dynam. Astron., 78, 17
Knežević Z., Milani A., 2003, A&A, 403, 1165
Lazzaro D., Angeli C. A., Carvano J. M., Mothé-Diniz T., Duffard R., Florczak M., 2004, Icarus, 172, 179
Lazzaro D., Carvano J. M., Hasselman P. H., Mothé-Diniz T., 2009, DPS, 41, 3407
Michel P., Benz W., Richardson D. C., 2004, Icarus, 168, 420
Michtchenko T., Lazzaro D., Ferraz-Mello S., Roig F., 2002, Icarus, 158, 343
Milani A., Farinella P., 1994, Nat, 370, 40
Milani A., Knežević Z., 1990, Celest. Mech. Dynam. Astron., 49, 347
Milani A., Knežević Z., 1992, Icarus, 98, 211
Milani A., Knežević Z., 1994, Icarus, 107, 219
Milani A., Nobili A. M., Knežević Z., 1997, Icarus, 125, 13
Morbidelli A., Guzzo M., 1996, Celest. Mech. Dynam. Astron., 65, 107
Morbidelli A., Nesvorny D., 1999, Icarus, 139, 295
Mothé-Diniz T., Roig F., Carvano J. M., 2005, Icarus, 174, 54
Tedesco E. F., Noah P. V., Noah M., Price S. D., 2002, AJ, 123, 1056
Tholen D. J., Barucci M. A., 1989, in Binzel R. P., Gehrels T., Matthews M. S., eds, Asteroids II. University of Arizona Press, Tucson, AZ, p. 298
Vokrouhlický D., Brož M., Bottke W. F., Nesvorný D., Morbidelli A., 2006, Icarus, 183, 349
Zellner B., Tholen D. J., Tedesco E. F., 1985, Icarus, 61, 355

This paper has been typeset from a TEX/LATEX file prepared by the author.